Steady film flow over a substrate with rectangular trenches forming air inclusions

S. Varchanis, Y. Dimakopoulos, and J. Tsamopoulos*
Laboratory of Fluid Mechanics and Rheology, Department of Chemical Engineering, University of Patras, Greece
(Received 1 September 2017; published 7 December 2017)

Film flow along an inclined, solid substrate featuring periodic rectangular trenches may either completely wet the trench floor (Wenzel state) or get pinned on the entrance and exit corners of the trench (Cassie state) or assume other configurations in between these two extremes. Such intermediate configurations are examined in the present study. They are bounded by a second gas-liquid interface inside the trench, which adheres to its walls forming two three-phase contact lines, and encloses a different amount of air under different physical conditions. The Galerkin finite-element method is used to solve the Navier-Stokes equations in a physical domain, which is adaptively remeshed. Multiple steady solutions, connected by turning points and transcritical bifurcations as well as isolated solution branches, are revealed by pseudo-arc-length continuation. Two possible configurations of a single air inclusion inside the trench are examined: the inclusion either surrounds the upstream convex corner or is attached to the upstream trench wall. The penetration of the liquid inside the trench is enhanced primarily by increasing either the wettability of the substrate or capillary over viscous forces or by decreasing the flow rate. Flow hysteresis may occur when the liquid wetting of the upstream wall decreases abruptly, leading to drastically different flow patterns for the same parameter values. The interplay of inertia, viscous, gravity, and capillary forces along with substrate wettability determines the volume of the air encapsulated in the trench and the extent of deformation of the outer free surface.

DOI: 10.1103/PhysRevFluids.2.124001

I. INTRODUCTION

Steady film flow of a Newtonian liquid over an inclined plane with variable topography is of great importance in various engineering applications. This is a basic model for coating and liquid film deposition processes, which is very widely used in fabrication of microelectronic components, integrated circuits, and other storage devices, such as magnetic discs and tapes, memory devices, optical discs, and photographic films. Such flows also arise in printing processes (e.g., gravure printing [1]) and in arrangements aiming at intensifying heat or mass transfer operations (e.g., two-phase heat exchangers and adsorption or distillation columns using structured packings; Argyriadi *et al.* [2]), falling film reactors and in many other applications (Craster and Matar [3]). Spreading of a liquid drop can take place by applying an external body force, either gravity or the centrifugal force. A popular process in electronics and optics industry is spin coating, where a substrate is covered by a blob of fluid under the impact of centrifugal force [4]. In the present work, gravity is the externally applied force. A common difficulty that appears is that substrates are not flat and their variable topography induces variations in the thickness of the deposited layer, as pointed out by Stillwagon and Larson [5]. There is need for more realistic representations of coating failures where the fluid does not cover completely the bottom of the topography, leading to the formation of gas inclusions between the coating layer and the substrate. Also, the wetting of the solid substrate depends on the advancing and receding contact angles, which are properties of the liquid, solid, and air. A nonuniform coating leads to low-quality products or to manufacturing

*tsamo@chemeng.upatras.gr

failures, which naturally are undesirable, because they let humidity get in contact with the printed circuits of the electronic boards leading to their corrosion and malfunction. Therefore, the film flow and film thickness have to be controlled to suppress the resulting nonuniformities or partial coatings [5].

So far, researchers have assumed almost exclusively that the film is in complete contact with the substrate (Mazouchi and Homsy [6], Kalliadasis *et al.* [7], Bontozoglou and Serifi [8]). Examining the possibility of having air entrapped inside the trench will, on one hand, facilitate understanding of the mechanisms that lead to nonuniform coating and, on the other hand, contribute important new ideas in another research area: In microfluidics, it is of great interest to determine conditions for drag reduction without chemically modifying the channel wall. Drag reduction can be achieved by a gaseous film somehow placed between the wall and the fluid (Tsai *et al.* [9]). Clearly, such a configuration is not stable in straight or smoothly varying substrates (Kouris and Tsamopoulos [10]). This led to the development of walls with periodic trenches up to a few tenths of μm in width and often larger depth, inside which air is entrapped, and, because of surface tension, liquid is not expected to penetrate the trench. As a result, the solid-liquid friction arises only in part of the confining wall where these two phases come in contact. These surfaces are called super-hydrophobic (Muralidhar *et al.* [11], Moulinet and Bartolo [12]). Immediately, it becomes apparent that several factors, such as the size, geometry, and direction of these trenches with respect to the flow, the liquid-solid affinity, the applied pressure from the liquid side, or from inside the trench, will play a crucial role in the development and maintenance of gas inclusions in the trenches.

Two extreme configurations of the liquid flowing over a trench have been routinely assumed: (i) The liquid fully displaces air from the trench, the so-called Wenzel state; and (ii) The liquid forms an interface with the air pinned at the two top corners of the trench, the so-called Cassie-Baxter or fakir state (Duez *et al.* [13]). Clearly, one can readily envision that between these two extreme states a host of others may arise in which the liquid-gas interface forms one or more contact points with the side walls or the bottom of the trench. Lampropoulos *et al.* [14] and Karapetsas *et al.* [15] recently investigated transient coatings of two-dimensional and three-dimensional rectangular trenches, respectively. They found that among the several possible coating failures of a trench, the following two seem to arise more frequently: the so-called capping failure, where the liquid fails to coat the trench, leaving entrapped air in the entire bottom of the trench and the bubble in the upstream corner configuration, where a large air inclusion is formed at the upstream corner of the trench. Recently, Pettas *et al.* [16] investigated the degree of wetting of a slit by a liquid film flowing along an inclined plane, which resembles the flow over a very deep rectangular trench. A more extensive literature review can be found in these three publications.

The main objective of this study is to develop an accurate and efficient numerical method to solve the steady thin film flow of a Newtonian film over a substrate with topography and to examine new possible film arrangements not studied so far by taking into consideration the existence of a bubble with two contact lines inside the trench. This will also definitively demonstrate that the widely used ideal Cassie state is not the only possible or the preferred arrangement, something that has been routinely assumed. The steady-state calculations are less expensive than the transient ones and able to cover adequately the multidimensional parameter space in this problem. We simplify the problem assuming that the primary direction of film flow is normal to the entrance of the rectangular trench, making the flow two-dimensional. The problem formualtion is given in Sec. II. The Galerkin finite-element method combined with a quasielliptic mesh generator (Dimakopoulos and Tsamopoulos [17]), to solve the full two-dimensional Navier-Stokes equations along with the continuity equation are described in Sec. III. Characterisitcs of the film arrangement and comparison with earlier studies are given in Sec. IV, followed by an extensive parametric analysis to study the effect of physical and geometric parameters on the free surface shapes and the resulting flow field in Sec. V. Conclusions are drawn in Sec. VI.

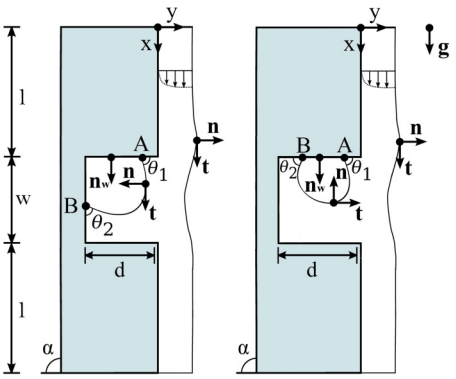

FIG. 1. Sketch of the film flow over a rectangle trench with air inclusion at the upstream corner (left) or at the upstream wall (right). The geometric parameters, the unit vectors on each surface and the contact points and angles are indicated. When the indicated lengths are dimensional, the film thickness in the entrance is H; when they are dimensionless, it is unity.

II. PROBLEM FORMULATION

A. Definition of the physical problem

We consider as a model system the steady, two-dimensional film flow of a Newtonian fluid on a plane inclined with respect to gravity by an angle α and featuring a trench. For the most part we will take $\alpha = 90^\circ$. The fluid is incompressible with constant density ρ, interfacial tension σ, and dynamic viscosity μ. The film of thickness H is flowing over the topographic feature with a sudden expansion in the flow cross-section, called a step-down hereafter, and located at distance l from the entrance. The trench that is formed has depth d and width w, while the distance from the sudden contraction, called a step-up hereafter, to the exit is l (see Fig. 1). The fluid is driven by the action of gravity generating a flux $q = UH$ where U and H are the characteristic velocity and the flat film thickness, respectively, far from the feature. The liquid may form with the solid an apparent contact angle θ, which is the angle between n_w, the unit normal vector to the solid wall, and the normal n to the visible free surface at a putative contact line. When the contact line is free to migrate, it prompts a sudden change from adherence at the solid surface to no shear along the free surface and induces a local singularity, which is known to be logarithmically weak and integrable (Michael [18], Richardson [19]). So the apparent contact angle is accepted as an overall measure of the wettability (Kistler and Scriven [20]), although different effects may influence this wetting measure (Johnson and Dettre [21], Oliver *et al.* [22], Teletzke *et al.* [23]). Figure 1 shows the flow geometry where the coordinates x and y originate at the intersection between the entrance plane and the upper flat wall and correspond to the local streamwise and its normal direction. The pressure of the entrapped air is a function of the initial conditions of the coating process. In this study, however, we directly solve for the steady-state arrangements and need to assume the pressure of the air inside the inclusion. To this end, this pressure is assumed to be equal to that of the ambient air. This particular choice is found to be valid, as explained by Young [24], and by examining the transient coating simulations of Lampropoulos *et al.* [14] and the simulations we present in Sec. IV C. One of the two liquid interfaces is the outer gas-liquid free surface and the other one is formed inside the trench between the contact lines A and B. Contact line A is allowed to migrate along the upstream wall of the trench, while contact line B is allowed to migrate either on the bottom wall of the trench (a bubble is formed in the upstream corner Fig. 1, left) or on the upstream wall of the trench (a bubble is formed in the upstream wall Fig. 1, right). These two bubble locations are favored over others, which were less often found by Lampropoulos *et al.* [14], simply because for hydrostatic reasons the pressure in the liquid is lower around the upper trench wall. The penetration of the liquid inside the trench as well as its impact on the deformation of the outer interface are investigated as well.

TABLE I. Properties of the glycerine-water mixture 98% at different temperatures.

T (°C)	σ (N/m)	ρ (kg/m^3)	μ (Ns/m^2)	Ka	l_c (mm)	l_v (mm)
10	0.0635	1290	0.245	2.10	2.240	1.543
20	0.0622	1260	0.0939	7.35	2.243	0.827
30	0.0620	1230	0.0409	22.02	2.267	0.483
40	0.0615	1200	0.0195	58.17	2.286	0.299

We scale all lengths with the film thickness H, and velocities with the cross-sectional average film velocity, U, at the entrance. In addition, both the pressure and stress components are scaled with a viscous scale, $\mu U/H$. Thus, the dimensionless groups that arise are the Reynolds number, $\mathrm{Re} = \rho U H/\mu$, the capillary number $\mathrm{Ca} = \mu U/\sigma$, and the Stokes number $\mathrm{St} = \rho g H^2/(\mu U)$. Note that at the inlet and the outlet the dimensionless film thickness is equal to unity due to our choice of characteristic scales. The capillary number is directly determined but not used, because a parameter which depends only on liquid properties, the Kapitza number $\mathrm{Ka} = \sigma \rho^{1/3} g^{-1/3} \mu^{-4/3} = (l_c/l_v)^2$ is preferred. This choice automatically determines the value of Ca via the expression

$$\mathrm{Ca}^{-1} = \mathrm{St}^{1/3} \mathrm{Ka}\, \mathrm{Re}^{-2/3}. \tag{1}$$

The capillary length l_c and the viscous length l_v are calculated by

$$l_c = \left(\frac{\sigma}{\rho g}\right)^{1/2}, \quad l_v = \left(\frac{\mu^2}{\rho^2 g}\right)^{1/3}. \tag{2}$$

We also define the Weber number, $\mathrm{We} = \rho U^2 H/\sigma = \mathrm{Re}\,\mathrm{Ca}$, a measure of the relative importance of fluid inertia compared to its surface tension, the Bond number, $\mathrm{Bo} = \rho g H w/\sigma$, a measure of the relative importance of the gravity force acting on the film (length scale, H, the film width) compared to the capillary force on the bubble inside the trench (length scale, w, the width of the trench). These dimensionless numbers will prove very useful in analyzing the flow patterns determined by our simulations.

By examining the model equations in dimensionless form, our results are applicable to a variety of liquids. Nevertheless, relating the values of the dimensionless parameters to actual liquids is certainly important. As an example, in Table I we present the physical properties of the glycerin-water mixture at different temperatures and how they affect the Kapitza number and the characteristic viscous and capillary lengths of the mixture. Varying the Reynolds number, i.e., the flow rate, affects the Nusselt film thickness H and the mean velocity U at the entrance of the liquid as depicted in Table II for a vertical substrate. H is calculated by the expression $(H/l_v)^3 = \mathrm{Re}\,\mathrm{St}$ and U from the definition of Stokes number St. We choose to examine cases where the height of the film at the entrance of the domain is up to 2 mm, because most of the industrial applications of this type of flow take place at film thickness up to this magnitude. In what follows all variables used will be dimensionless.

TABLE II. Variation of the length and velocity scales for $l_v = 0.483$ mm.

Re	St	H (mm)	U (mm/s)
0.1	3	0.323	10.27
1	3	0.697	47.74
10	3	1.50	221.47

B. Governing equations and boundary conditions

The two-dimensional steady-state flow is governed by the laws of mass and momentum conservation,

$$\nabla \cdot \mathbf{u} = 0, \tag{3}$$

$$\mathrm{Re}\,\mathbf{u} \cdot \nabla \mathbf{u} - \nabla \cdot \mathbf{T} - \mathrm{St}\,[g \sin(\alpha)\mathbf{e_x} - g \cos(\alpha)\mathbf{e_y}] = \mathbf{0}, \tag{4}$$

where the total stress tensor is defined as $\mathbf{T} = -p\mathbf{I} + (\nabla \mathbf{u} + \nabla \mathbf{u}^T)$ and $\mathbf{u} = (u, v)^T$ and p are the velocity vector and pressure fields.

Along the two shear-free air-liquid interfaces, the dynamical condition is imposed to balance the capillary force and normal stress with the ambient air pressure, p_a, which is set to zero as the datum pressure,

$$\mathbf{n} \cdot \mathbf{T} = -p_a \mathbf{n} + \mathrm{Ca}^{-1} \frac{d\mathbf{t}}{ds}, \tag{5}$$

where $\mathbf{n}$ is the outward unit vector to the free surfaces and $\mathbf{t}$ is the unit tangent vector pointing in the direction of the increasing distance s along the free surfaces (Ruschak [25]). The interface shape obeys the kinematic condition, which in a steady-state requires setting the normal component of velocity to zero,

$$\mathbf{u} \cdot \mathbf{n} = 0. \tag{6}$$

At the two intersections of the inner interface (its unit normal vectors denoted as $\mathbf{n}_{s1}$, $\mathbf{n}_{s2}$) with the two trench walls (their unit normal vectors denoted as $\mathbf{n}_{w1}$, $\mathbf{n}_{w2}$), the following equations are imposed allowing the contact lines to move along the walls,

$$\mathbf{n}_{s1} \cdot \mathbf{n}_{w1} = \cos\theta_1, \tag{7}$$

$$\mathbf{n}_{s2} \cdot \mathbf{n}_{w2} = \cos\theta_2. \tag{8}$$

Because of the complex pattern of slow recirculation flow inside the trench, the contact lines A and B may have the role of either a receding or an advancing contact line, as in Ref. [16]. Moreover, it will become clear in the results section that the flow inside the trench and especially closer to the contact lines is much slower than the flow in the rest of the film. Thus, it is reasonable to neglect the specific role of each angle and assume that they have the same equilibrium value θ, characterizing the specific liquid/solid pair; i.e., we set $\theta_1 = \theta_2 = \theta$. This also allows us to carry out the parametric simulations in terms of just one equilibrium contact angle θ and investigate its role on the flow. On all walls of the topographic feature we impose the usual no slip and no penetration conditions:

$$\mathbf{u} = \mathbf{0}. \tag{9}$$

Boundary conditions must be also applied at the entrance and exit of the flow domain. The periodicity of the substrate geometry irrespective of its particular features allows us to impose periodicity between the inflow and the outflow boundaries in all primary variables. In particular, we apply periodicity on both the streamwise and normal velocity components, on the pressure as well as on the location of the fluid-air interface in the usual manner; see, for example, Kouris and Tsamopoulos [26] and Pozrikidis [27]. Moreover, we choose to impose periodicity, to avoid the requirement of fully developed flow at the inlet and the outlet. If the distance of the feature from the inlet and outlet is large enough, the flow will be fully developed, the normal velocity will vanish, while the streamwise one will depend only on the normal to the wall direction and the periodic conditions will reproduce the steady solution derived by Pavlidis *et al.* [28]. To achieve this, we have chosen $l = 15$. The Stokes number, St, which appears in the above equations is determined by

requiring that the dimensionless, average film-velocity, or the dimensionless flow rate $\tilde{q}$, are equal to unity, since the mean velocity at the inflow boundary is used as a characteristic velocity for making the model equations dimensionless. Therefore, the additional equation that arises is

$$\tilde{q} = \int_0^1 u dy = 1. \tag{10}$$

The Stokes number depends strongly on the rheological properties of the material and it is computed as part of the solution. For fully developed flow of Newtonian fluid over a vertical wall, the well-known Nusselt solution is recovered, where the uniform film thickness is $H = (3\mu q/\rho g)^{1/3}$, q is defined as the dimensional volumetric flow rate per unit span. Then, $\mathrm{St} = 3$, as discussed in Ref. [28].

III. COMPUTATIONAL METHOD

A. Elliptic grid generation and mixed finite element method

The mixed Galerkin finite-element method is used to solve numerically the governing equations. The mesh is generated by solving the system of two quasielliptic partial differential Eqs. (11) and (12), which map the physical domain (x,y) to the computational domain (ξ,η), and it is dynamically adapted to the deforming liquid domain. This procedure has been advanced by Dimakopoulos and Tsamopoulos [17] and subsequently applied in various geometries and problems; e.g., see Refs. [29,30]. The mesh generation equations are

$$\nabla \cdot \left\{ \left[\varepsilon_1 \sqrt{\frac{x_\eta^2 + y_\eta^2}{x_\xi^2 + y_\xi^2}} + (1-\varepsilon_1) \right] \nabla \xi \right\} = 0, \tag{11}$$

$$\nabla \cdot \left\{ \left[\varepsilon_2 \sqrt{\frac{x_\xi^2 + y_\xi^2}{x_\eta^2 + y_\eta^2}} + (1-\varepsilon_2) \right] \nabla \eta \right\} = 0, \tag{12}$$

where the parameters ε_1 and ε_2 control the smoothness and orthogonality of the mesh lines and ε_1, ε_2 are selected by trial and error. Following a triangulation, the mesh consists of only triangular elements, each one of which has three vertex nodes and three midedge nodes. The velocity and coordinate vectors are then represented elementwise in terms of six-node Lagrangian basis functions ($K = 6$) and the pressure in terms of three-node Lagrangian basis functions ($L = 3$),

$$\mathbf{u} = \sum_{i=1}^{K} \mathbf{u}_k \varphi^k(\xi,\eta), \quad \mathbf{x} = \sum_{i=1}^{K} \mathbf{x}_k \varphi^k(\xi,\eta), \quad p = \sum_{i=1}^{L} p_l \psi^l(\xi,\eta). \tag{13}$$

The number of total degrees of freedom must be equal to the total number of discretized equations. So, these basis functions are employed, respectively, as weighting functions for the momentum, grid-generating, and continuity equations in the weak formulation of the problem. The number of resulting residual equations is equal to the number of the nodal unknown variables u^i, v^i, p^j, x^i, and y^i (forming the unknown variable vector $\mathbf{S}$). To trace the steady-state solution vector ($\mathbf{S}$), the pseudo-arc-length continuation (Doedel *et al.* [31]) is incorporated into the finite-element code. Given an initial solution ($\mathbf{S}_0$) at an initial parameter value (λ_0), the value of the parameter λ for the next computation is unknown *a priori*, but a function of the pseudo-arc-length s_a. The inner product between the derivative of the initial solution with respect to pseudo-arc-length ($\dot{\mathbf{S}}_0$) and ($\mathbf{S} - \mathbf{S}_0$) is added to the product of the derivative of the initial value of the parameter with respect to pseudo-arc-length ($\dot{\lambda}_0$) and ($\lambda - \lambda_0$) and set to be equal with the pseudo-arc-length Δs_a to produce the additional equation G (14),

$$G(\mathbf{S},\lambda,\Delta s_a) = \dot{\mathbf{S}}_0^T \cdot (\mathbf{S} - \mathbf{S}_0) + \dot{\lambda}_0(\lambda - \lambda_0) + \Delta s_a = 0. \tag{14}$$

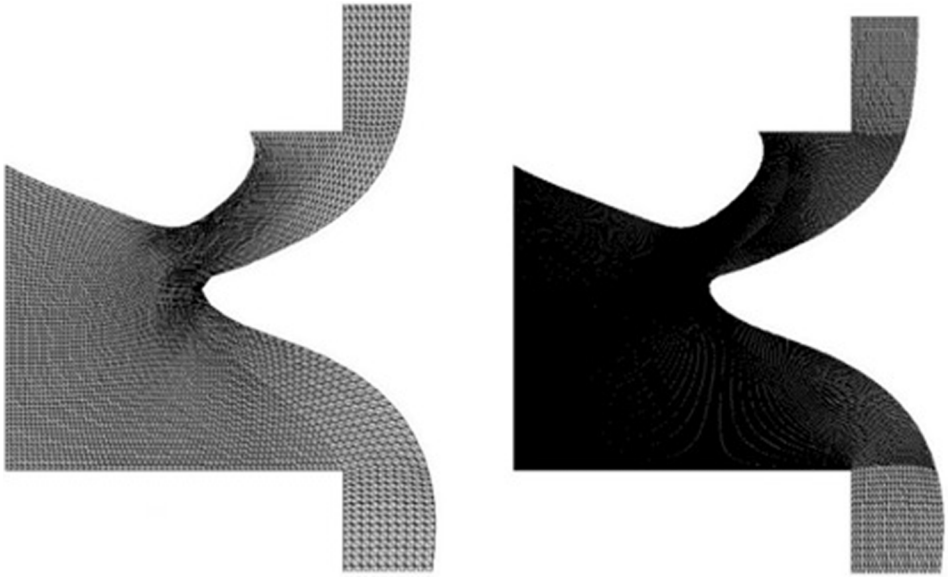

FIG. 2. Part of the mesh around the trench in the physical domain before (left) and after the remeshing (right). Here the two contact points are on the upstream side wall and the bottom of the trench.

The system of equations is solved by the Newton-Raphson iteration method. The Jacobian matrix of all residual equations except for Eqs. (10) and (14) is a banded matrix that can be stored by three single-index arrays according to the so-called compressed sparse row (CSR) format and solved with a sparse matrix solver (Watson package, Gupta [32]). However, these two equations, in particular, have a different structure because they involve several additional terms. If they were incorporated into the system and solved simultaneously, they would destroy the sparsity of the Jacobian in the CSR format. The way around this is to apply a special algebraic procedure (Zacharioudaki *et al.* [33]) to solve first for the two extra global variables, which are the Stokes number and the unknown value of parameter λ in the arc-length continuation.

Another crucial feature of this partial penetration problem is that the elements of the mesh suffer from large anisotropic deformations during parametric continuation, often making the Jacobian matrix singular. For different values of the parameter the free surfaces change shape and length, but the number of elements mapping the gas-liquid interfaces remain the same. As a result, the elements become much larger in one of the directions adding error to the transformation and after a few steps leading to divergence of the Newton-Raphson scheme. To cope with this problem, we used an adaptive remeshing algorithm that can add elements in the outer or inner free surface, if needed, preventing the boundary elements from becoming very large in one direction, thus conserving the high quality of our mesh as it can be seen in Fig. 2. The interested reader may refer to Refs. [16,29,30] for more details.

With regard to the accuracy of the numerical results reported in this paper, we performed mesh convergence tests to assure that our solution converges. A very efficient way to do so in this problem is by observing the position of the two contact lines with consecutively finer meshes, as this is the most sensitive and important feature of this problem. In all cases examined, we used meshes in which doubling the number of their elements resulted in error less than 10^{-2} dimensionless film thickness units in the position of the contact lines, before and after the remeshing. Different mesh sizes were used in each simulation; the trench size mainly defines the number of the elements in each mesh, as well as the deformation of the outer and inner free surface. A typical mesh for a trench whose dimensions are $l = 15$, $w = 5$, and $d = 5$ consists of about 20 000 triangular elements.

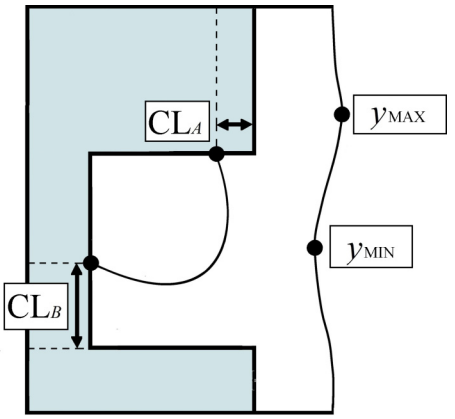

FIG. 3. Characteristic measures of film deformation.

IV. PRELIMINARY CONSIDERATIONS

A. Characteristic measures of film deformation

The results that follow will be presented in terms of pressure and stream function contours as well as in terms of the liquid penetration in the trench. A measure for estimating the overall liquid penetration and the amount of entrapped air is the position of contact lines A and B. As mentioned above, the position of contact line A (will be denoted as CL_A from now on) in the upstream wall of the trench is measured using as a reference point the upstream convex corner of the trench, while the position of contact line B (CL_B) is measured using as a reference point the downstream concave corner of the trench as it can be seen in Fig. 3. Another characteristic feature of this flow is the deformation of the outer gas-liquid interface, which is determined by the difference between its maximum and minimum heights. In particular, before a step down the so-called "capillary ridge" (Mazouchi and Homsy [5]) is formed and before a step up a capillary depression arises. An important feature of the film flow is the magnitude of the capillary ridge and the capillary depression, because the former drives the liquid inside the trench by capillarity and the latter decelerates it before it can flow around the downstream corner. A compact form for presenting these two geometric characteristics of the film is by defining the deformation amplitude of the outer free surface:

$$A_d = \frac{y_{MAX} - y_{MIN}}{2} \tag{15}$$

Where y_{MAX} denotes the y coordinate of the maximum height and y_{MIN} denotes the y coordinate of the minimum height of the outer interface.

B. Comparison with previous simulations

The predictions of the present work were compared with the results of Lampropoulos *et al.* [14], who performed transient simulations of gravity-driven viscous films over substrates with rectangular topographical features. Using the VOF method implemented in the OpenFoam software package they found that the transient coating process does not lead always to full coating; air inclusions of various sizes can be formed and sustained as the system reaches a steady state. The study presented in this paper, on the other hand, is a steady-state analysis aiming at more thoroughly and accurately examining the different film arrangements for different parameter values. We need to compare our results with those from transient simulations, because, to our knowledge, they are the only ones available in the literature. To this end, we have to make sure that the VOF simulations have reached a steady state. In Fig. 4 we present such a comparison between the predicted steady state (a) by Lampropoulos *et al.* [14] when this is achieved at $t = 265.7$ and (b) by this work for

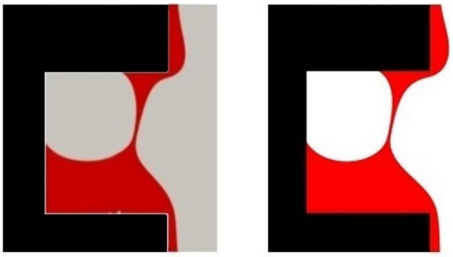

FIG. 4. Comparison of transient VOF simulations in OpenFoam by Lampropoulos *et al.* (a) with our predictions (b) for $\mathrm{Re} = 5.5 \times 10^{-4}$, $\mathrm{Ka} = 0.139$, $\theta = 30^{\circ}$, $w = 14$, and $d = 12.2$.

$\mathrm{Re} = 5.4 \times 10^{-4}$, $\mathrm{Ka} = 0.139$, $\theta = 30^{\circ}$, $w = 14$, and $d = 12.2$. One has to take into account that VOF computes the velocity field in both the air and the liquid assuming them to be a single material and accounting for a smooth change in the relevant physical properties. Moreover, it determines the liquid-air interfaces *a posteriori* locating them approximately within an element, see for example, Fraggedakis *et al.* [34]. In spite of this decreased accuracy of VOF, we can observe that the results are in very good agreement. In Table III we can see that the positions of either contact line have a relative error of less than 0.08 dimensionless length units. This error could be attributed additionally to the fact that Lampropoulos *et al.* [14] used curved convex corners in the trench to facilitate the transient computations, while we use sharp corners in our simulations.

Apart from validating our numerical method, this comparison can be very useful in this study since it can give information about the stability of the steady states we track. The fact that transient simulations lead only to stable steady states implies that the steady solution we have found, as well as neighboring solutions of the same solution branch are also stable and can be observed in coating processes over structured topography. Furthermore, our assumption that the entrapped air is in the same pressure with the ambient air is reaffirmed, because in the simulation of Lampropoulos *et al.* [14] shown in Fig. 4(a), they found that the pressure of the air inside the air inclusion (bubble in upstream corner) is less than 0.3 Pa smaller than the ambient pressure.

C. Pressure inside the air inclusion

As we have mentioned in Sec. II, the value of pressure inside the air inclusion is an extra unknown of this problem. However, estimating the value of the pressure is not possible in the present steady-state calculations, since it depends on the initial conditions of the transient coating problem and requires transient simulations. Setting the pressure of the air allowed us to perform simulations using hydrophilic substrates for the bubble in the upstream concave corner case and the bubble in the upstream wall case, as the pressure near the upstream wall is lower than the ambient pressure and a mean curvature of the inner free surface can be supported. Again, this assumption is consistent with the simulations of Lampropoulos *et al.* [14] and Karapetsas *et al.* [15] who found in their transient coating simulations that when large air inclusions are formed at the upstream corner of the trench, the pressure of the entrapped air is almost equal to that of the ambient air. It is interesting though, to examine the limitation of this simplification.

TABLE III. Relative error in the position of contact line A and B between this work and Ref. [13].

	Position of contact line A, CL_A	Position of contact line B, CL_B
Lampropoulos *et al.* [13]	4.4811	7.0402
This work	4.8638	6.9598
Relative error	− 0.0787	+ 0.0116

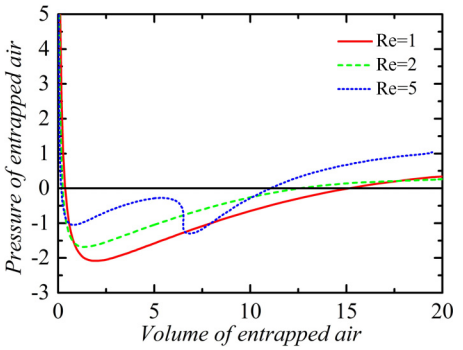

FIG. 5. Dependence of the pressure inside the air inclusion on the volume of air inside the air inclusion for different values of the Reynolds number, Ka $= 2$, $\theta = 60^\circ$, $d = 5$, and $w = 5$.

To do so, along with the already presented governing equations of the physical problem, we solve an additional equation by which we impose the volume of the air inclusion when it is located at the upstream corner of the trench. The unknown of this extra equation is the pressure of the air inclusion. As it can be seen in Fig. 5, we carry out continuation in the volume of the air inclusion for various values of the Reynolds number. We can observe that for air inclusions with volume larger than 0.1 dimensionless units there is a small deviation (up to 2 dimensionless pressure units) of the absolute value of the pressure inside the air inclusion from the ambient pressure value. Since in this study we are interested in air inclusions that can be comparable to the trench dimensions and affect the coating quality, setting the pressure inside the air inclusion equal to the ambient air is a very good approximation. In addition, this is a necessary simplification, because the purpose of this work is to estimate the volume of the air inclusion under parameters that can be controlled in the physical problem such as the flow rate, the dimensions of the trench, the coating liquid, etc. We also performed numerous simulations using different values of the pressure inside the air inclusion, ranging from -2 to 2 dimensionless units and altering the Reynolds number. We found that they produced insignificant changes to the physical phenomena that take place. As noted by one of the reviewers, setting the pressure in the bubble to the ambient pressure could be achieved experimentally by a very small ventilation hole on the trench wall, which does not permit liquid penetration. Therefore, all the simulations presented subsequently were performed considering that the pressure of the entrapped air is equal to that of the ambient air.

V. NUMERICAL RESULTS AND DISCUSSION

A. Bubble in upstream corner case

1. Flow and pressure fields

First, it is useful to examine the flow field in detail especially for the liquid near and inside the trench. The streamlines and the pressure field at Re $= 1$ are shown in Figs. 6(a) and 6(b). At this flow rate the liquid wets slightly the upstream wall and the film falls almost vertically above the trench. Note that the two contact angles do not necessarily assume their expected function (because of their position), as an advancing or receding contact angle, but their function depends also on the existence or not of recirculation nearby. This was one of the reasons we assumed $\theta_1 = \theta_2 = \theta$. The liquid enters the trench by wetting the upstream wall. Further downstream it forms a neck, which induces a maximum in the x velocity, while the y velocity is almost zero. After that point, the liquid decelerates as it approaches the downstream wall. The decrease in the streamwise velocity is accompanied by a sharp rise in the y velocity in order for the liquid to exit the trench and satisfy the mass balance. The film is split in two regions: the outer one, which continues its steady flow over the trench, and the inner one, in which the fluid just recirculates remaining in contact with the downstream trench wall.

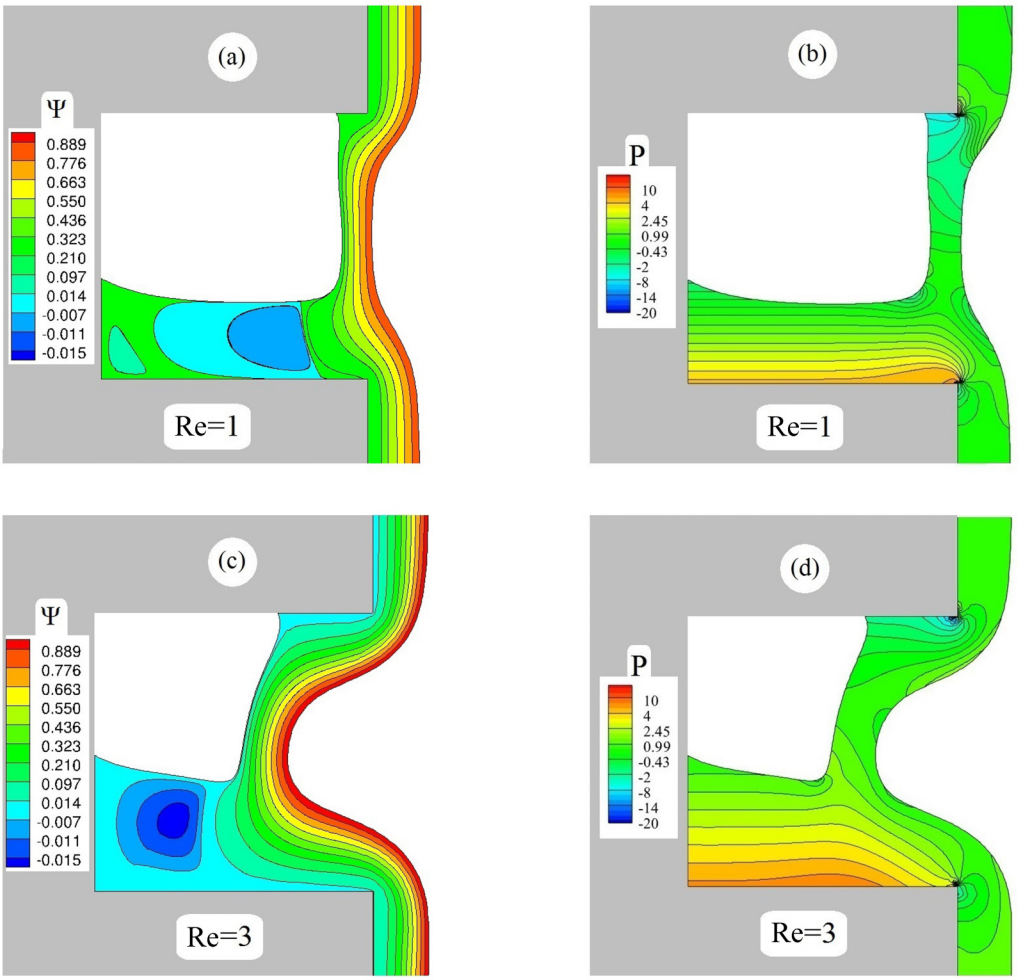

FIG. 6. Close-up views around the trench and just before and after it showing the streamlines and the pressure field, respectively, for two values of Reynolds number: (a), (b) Re = 1, (c), (d) Re = 3 at parameter set Ka = 2, $\theta = 60^\circ$, $w = 5$, and $d = 5$, with $l = 30$.

A streamline separates the two regions and liquid particles in the two regions do not communicate. The former region is also bounded by the outer and inner film interface. In the recirculation region, the velocities are at least two orders of magnitude lower than those in the outer region. The pattern of recirculation that is formed resembles the so-called Moffatt eddy pattern [35]. Despite the fact that in the 1D Nusselt flow there is no pressure variation, i.e., the pressure in the liquid is uniform and equal to the pressure of the ambient air, in Fig. 6(b) we can see that the pressure follows an almost hydrostatic variation inside the trench, except near the its two vertices in its entrance and exit, where it increases abruptly. This hydrostatic variation can be justified by observing that the inner, very slowly moving fluid is not affected by the rest of the falling film. In the middle of the neck, the pressure is almost the same with that of the ambient air and the y component of velocity is almost zero; the flow there approaches the perfect plug flow.

At higher Reynolds number Re = 3 [Figs. 6(c) and 6(d)], the contact line A is located deeper in the trench, still the film does not penetrate much into the trench and again forms a large air inclusion around the upstream concave corner. The plug flow profile in the middle of the neck has disappeared, as the film is deflected from its vertical fall significantly. The mean curvature of the outer free surface

is greater to support the sharp changes in the direction of the velocity vector as the liquid enters and exits the trench. The recirculation area is observed to shrink near the downstream concave corner which is a result of the longer wetting of CL_A and the consequent inward deflection of the film. The dividing streamline seems to be a direct extension of the inner interface of the film. This locally increases the curvature of the inner surface, tending to form a cusp. With regard to CL_B, we can observe that it is located in the recirculating area where the flow is very slow, balancing the gravity force which pulls the stagnant liquid downwards with the tendency of the hydrophilic contact line B to advance upwards. This resembles the capillary rise in a tube made of hydrophilic material. As the width of the recirculating region is reduced, the free surface is located higher, because the capillary effect dominates gravity. A small increase in the pressure is observed exactly at the point where the flow is separated from the recirculating eddy on the downstream wall, which is very reasonable, because a stagnation point is located there and greater velocity leads to greater pressure at that point.

2. Inertial effect

To examine the dependence of the solution family on the Reynolds number, Fig. 7 depicts the wetting lengths CL_A, CL_B and the deformation amplitude A_d along with insets of film arrangements with streamline patterns. At least two steady states coexist for most of the range of Re where we performed simulations, composing two solution branches: a branch in which the flow profiles feature deep penetration of the liquid in the trench leading to almost full coating with a tiny air inclusion (this will be called the "upper" branch from now on) and a branch in which the liquid penetrates partially the trench forming a large air inclusion (this will be called the "lower" branch from now on). These two branches are connected at a turning point at $\mathrm{Re} \approx 0.18$ and solutions of this type (bubble in upstream corner) cease to exist for this set of parameters below this value of Reynolds number. This fact stems from the definition of the capillary number. It is easy to see that when $\mathrm{Re} \to 0$ results in $\mathrm{Ca}^{-1} \to \infty$ [Eq. (1)], thus no solution can exist for $\mathrm{Re} = 0$. According to bifurcation theory [36], a real eigenvalue of the system changes sign at the turning point. Given that the transient simulations of Lampropoulos *et al.* [14] for a different trench geometry converge to the corresponding steady-state families on the lower branch even near the turning point (see Fig. 3), the present solutions are expected to be stable. A more comprehensive study of the linear stability of the steady states to even time periodic or three-dimensional disturbances is beyond the scope of the present study, but will be reported in a forthcoming study.

First, we examine the lower branch following the change of the flow profile with increasing inertia or flow rate starting with $\mathrm{Re} = 1$. We note that the wetting distance of CL_A and CL_B as well as the deformation amplitude of the outer free surface A_d tend to increase until a maximum is reached for CL_A and A_d. Then we can observe two successive turning points defining a hysteresis loop at about $\mathrm{Re} \approx 3.9$, which resembles the hydrodynamic hysteresis that Kistler and Scriven [20] observed in the so-called teapot effect, and also the hydrodynamic hysteresis Pettas *et al.* [16] found when examining the flow of a liquid film over an inclined plane with a slit. This hysteresis does not affect as much the location of CL_B. At even higher flow rates, CL_A tends to become pinned on the convex upstream corner, but the solution family ends before $CL_A = 0$. For this set of parameters, we could not perform parametric continuation on the lower branch for $\mathrm{Re} > 6.3$, because of numerical difficulties generated by the cusp formed on the inner gas-liquid interface at the point where the falling film meets the recirculating liquid, which deforms too much elements nearby, making the Jacobian of the transformation singular. The formation of this cusp at the lower part of the inner interface could be a genuine physical limit, possibly signifying the onset of air entrainment from the bubble into the liquid. However, such flow configurations could not be tracked by our steady-state numerical scheme, because they are transient phenomena.

Second, examining the upper branch, we can see that the positions of contact lines A and B vary only slightly, always remaining near the upstream concave corner. On the other hand, the deformation amplitude of the outer interface is affected significantly by the change on the flow rate at about $\mathrm{Re} \approx 9.8$, where a second hysteresis loop arises leading to a less deformed outer air-liquid interface as well as the onset of an "inertia ridge" at the exit of the trench. It is very interesting that

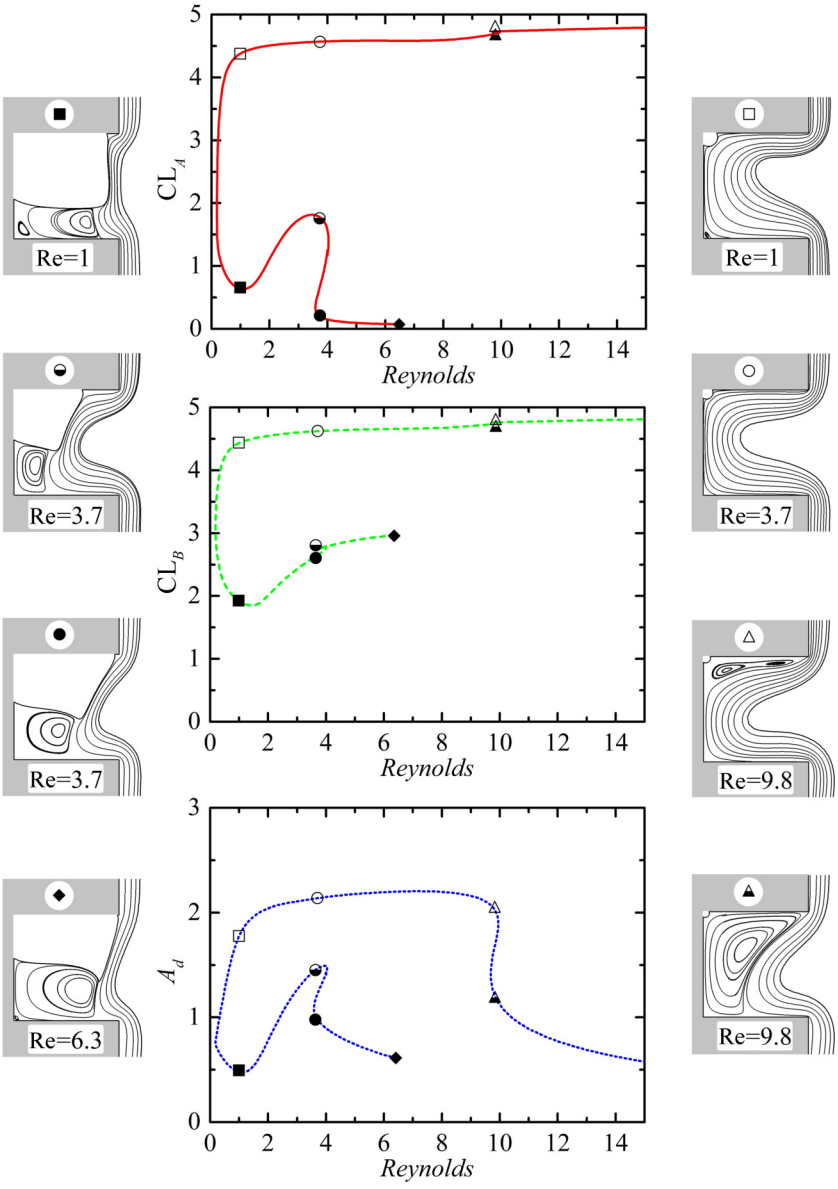

FIG. 7. Map of the steady-state solutions in terms of the wetting of contact line A (CL_A), contact line B (CL_B), or the deformation amplitude (A_d) for Ka $= 2$, $\theta = 60^\circ$, $d = 5$, and $w = 5$. Here and in similar figures that follow the symbols in the solution family correspond to one of the flow patterns around the three figures.

both CL_A and CL_B are only slightly affected by this major change in the flow pattern and the shape of the outer interface.

Observing the continuation curves and the flow patterns we can define three flow regimes: at low inertia (Re < 1), the dominant forces are gravity and capillarity defining a capillary-gravity region, while at high values of flow rate (Re > 4) inertia dominates capillarity leading to an inertia-gravity driven flow. For the range $1 <$ Re < 4, a competition between the capillarity, viscous, and inertia forces takes place as the film arrangement moves from one region to the other giving rise to the hydrodynamic hysteresis on the lower branch. Next, we will examine each region separately.

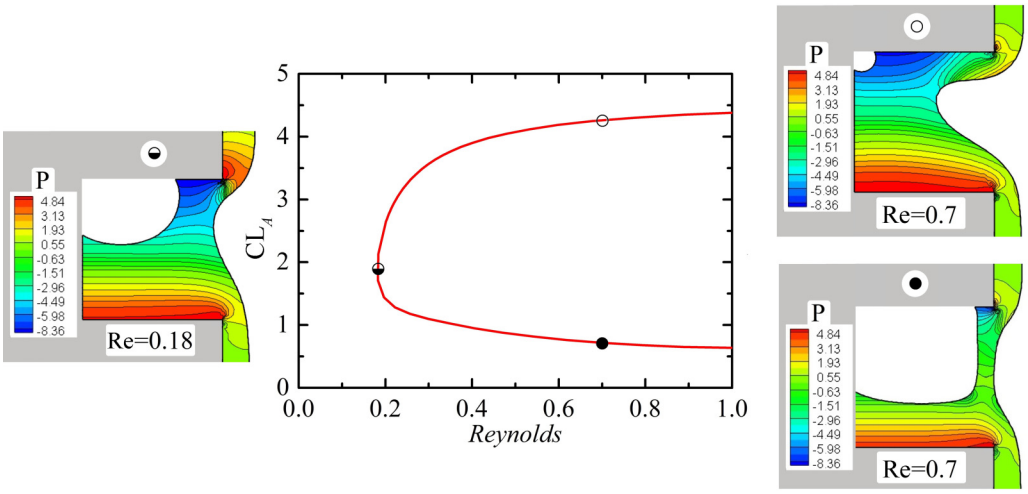

FIG. 8. Enlarged capillary-gravity region for Ka $= 2$, $\theta = 60^\circ$, $d = 5$, and $w = 5$ along with contours of the pressure field for Re $= 0.18$ and Re $= 0.7$.

3. Capillary-gravity region

This part of the solution branches and the related film shapes with the pressure contours are depicted in Fig. 8. Starting from the minimum wetting length of CL_A, which arises for Re ≈ 0.96 or Bo ≈ 5 (this is the upper bound of the capillary-gravity region) and decreasing the flow rate we can see an increase in the wetting length of CL_A. This can be explained by the fact that with decreasing Re, Ca decreases as well [Eq. (1)], making the capillary force the dominant one to be balanced by gravity. This makes the decreasing Bond number, the more relevant parameter in this range. The increased capillarity in the normal stress balance [Eq. (5)] can be equilibrated only by an increased pressure jump across the inner air-liquid interface. This is achieved by the shrinkage of the air inclusion to increase its surface curvature and by its migration towards the upstream wall where the pressure is considerably lower. Overall, CL_A translates deeper in the trench and a pressure gradient arises in the film along the upstream wall, which pulls the liquid into the trench, thus amplifying the deformation of the outer gas-liquid interface; see Fig. 8. As a result, the stagnation point, which separates the recirculating region from the outer film flow, is moved deeper into the trench making the recirculation region narrower. In accordance with the capillary tube phenomenon, the CL_B wetting length increases as capillarity becomes more important than gravity in the recirculating liquid region. This trend remains in effect until Re ≈ 0.18, where a saddle-node bifurcation takes place and no steady states of this type exist below this value of flow rate.

As can be seen in Figs. 7 and 8, another solution branch also exists in this region in which the flow approaches full coating. Here the air inclusion is even smaller generating an even higher pressure decrease in the liquid side of the inner interface. The increased pressure gradient within the film near the upstream wall pulls the outer free surface towards the trench deforming it considerably. No recirculation region exists (see Fig. 7). In other words, in this branch, the fluid that enters the trench pushes the air inclusion deeper in the trench. In contrast to the lower branch, here we can observe that with increasing Re the air inclusion decreases monotonically. In fact, the air inclusion attains an almost circular cross section (mean curvature $\approx 1/R_{\text{air inclusion}}$) and shrinks, to maintain the balance between capillarity and the pressure jump term across the inner air-liquid interface. The fact that we cannot find a solution of this type for Reynolds less than 0.18, for this set of parameters, is in accordance with the flow maps of Gramlich *et al.* [37] who found full coating of the substrate in the absence of inertia for Ca $= 0.1$, $d = 5$, $w = 5$ in their transient simulations.

4. Transition region

In Fig. 7 we observed that increasing Re above unity results in deeper penetration of the liquid in the trench, as both CL_A and CL_B increase even in the lower branch. While inertia is becoming more significant than capillarity and viscous forces, the capillary ridge above the trench entrance vanishes and an inertia ridge appears before the trench exit. The decrease of the capillary ridge decreases the capillary pressure it generates driving the film inside the trench. Now it is the capillary force by the inner interface near CL_A and the pressure gradient it generates as well as the wall hydrophilicity the mechanisms producing this result. In contrast to what one could have expected, increasing Re above unity leads to CL_A migrating deeper in the trench. This awkward development of the flow is attributed to the fact that with increasing Re, inertia becomes more significant than viscous forces, so the viscous resistance to the advancing of CL_A decreases allowing CL_A to advance deeper in the trench. With CL_A located deeper in the trench the pressure gradient below the upstream corner increases pulling more liquid inside the trench. Thus, a raise in the y component of velocity is triggered, leading to a sharp change in the direction of the velocity vector as the film enters the trench. This change generates increased values of the components of the stress tensor, which in turn along with the pressure variation provoke an intensified deflection of the outer free surface. The minimum of the outer gas-liquid interface moves deeper in the trench and closer to the downstream wall as the flow rate increases. This can be explained again by the ballistic effect, as explained for coating flows over sinusoidal topographies by Nguyen and Bontozoglou [38]. Monitoring the trajectory of a single particle flowing in the outer film region as it is being ejected from the substrate wall inertia and gravity pull it downwards, while the pressure gradient caused by the contact line A pulls it inside the trench. At low flow rate the particle lands closer to the upstream wall, while with increasing flow rate it lands closer to both the bottom of the trench and the downstream wall; this explains the observation that the minimum of the outer free surface is moved deeper in the trench and closer to the downstream wall as Re increases (compare the first two insets in the left side in Fig. 7).

This trend continues until, at a critical value of the Reynolds number, $\mathrm{Re} \approx 3.5$, CL_A reaches a maximum wetting distance. At this point inertia along with gravity have grown enough and the particles flowing at the outer region are less affected by the pressure gradient in the upper wall, which pulls them inside the trench and more affected by the adverse pressure generated at the stagnation point in the lower wall. This outward displacement of the film increases again the domain of recirculating liquid, Fig. 9. Overall, the minimum of the free surface is moved rather closer to the downstream wall rather than deeper in the trench. Slight increase of the flow rate from its value at the maximum in CL_A leads to a chain reaction of the effects discussed above as the particles are no more affected by the hydrophilic contact angle and the hysteresis loop is reached with the abrupt dewetting of the upstream wall and the so called "jump" in the wetting distance of CL_A and the deformation amplitude of the outer free surface A_d. In the new flow pattern, inertia is clearly dominant, the outer free surface is less deformed featuring an inertia ridge and CL_A is almost pinned to the upstream convex corner. The system reaches a new state with reduced drag force, as the wetting distance of CL_A is reduced by an order of magnitude and the liquid barely enters the trench while the outer gas-liquid interface is considerably flatter letting the liquid pass quickly from the outer region (see inset in the bottom right of Fig. 9).

The stability of the film arrangements around the hysteresis loop can be inferred using simple bifurcation ideas [36]. As explained earlier, while Re increases from unity the steady solutions are stable until the limit point is reached at $\mathrm{Re} \approx 4$. Moving further along this solution family the solutions are unstable until the second limit point is reached. From thereon it is likely that they will be stable again. A definitive answer can be obtained by performing a linear stability analysis, although the transient simulations [14,15] indicate that they are indeed stable.

5. Upper-branch hysteresis at high Reynolds numbers

As we have already mentioned, on the upper branch a hysteresis loop arises at $\mathrm{Re} \approx 9.8$, which is clearer by examining the variation of A_d in Fig. 7. Increasing the flow rate in the upper branch,

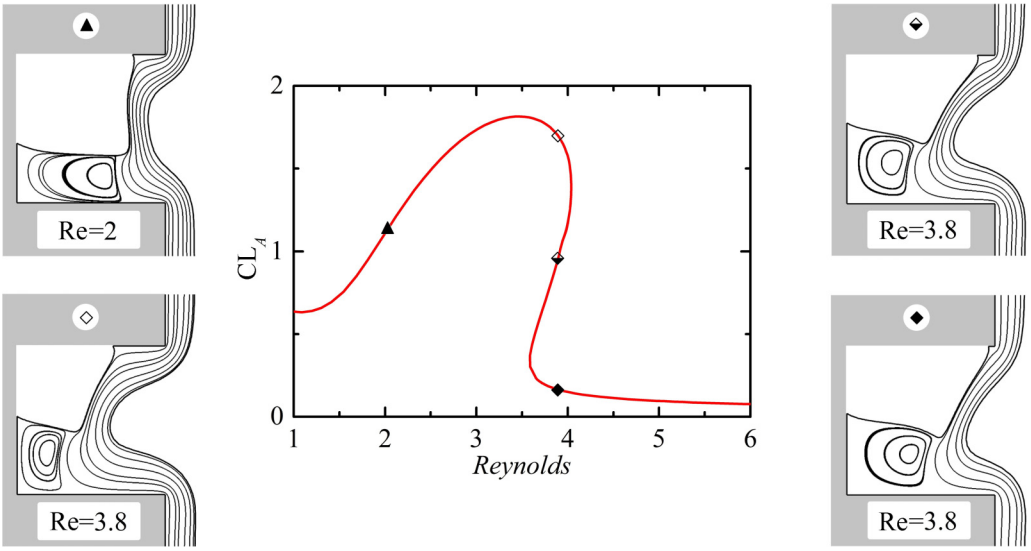

FIG. 9. Enlarged transition zone (lower branch) for Ka $= 2$, $\theta = 60^\circ$, $d = 5$, and $w = 5$ along with contours of the stream function for Re $= 2$ and Re $= 3.8$.

see also Fig. 10, we observe that the minimum of the outer free surface is moved deeper and closer to the downstream wall. This variation in the film shape decreases the cross-section through which the liquid enters and exits the trench, increases the y component of the velocity and moves deeper in the trench the stagnation point at the downstream wall. The pressure around the stagnation point increases, as can be seen in Fig. 8 pushing the outer free surface away from the trench and leading to a pure inertia-gravity dominated flow with a large recirculation inside the trench (see also Fig. 7), like the patterns observed at high inertia for full coating flows by Serifi and Bontozoglou [8]. Similar to the hysteresis in the lower branch, the abrupt decrease in the deformation amplitude around the upper-branch hysteresis is related to the fluid elements landing further downstream as inertia

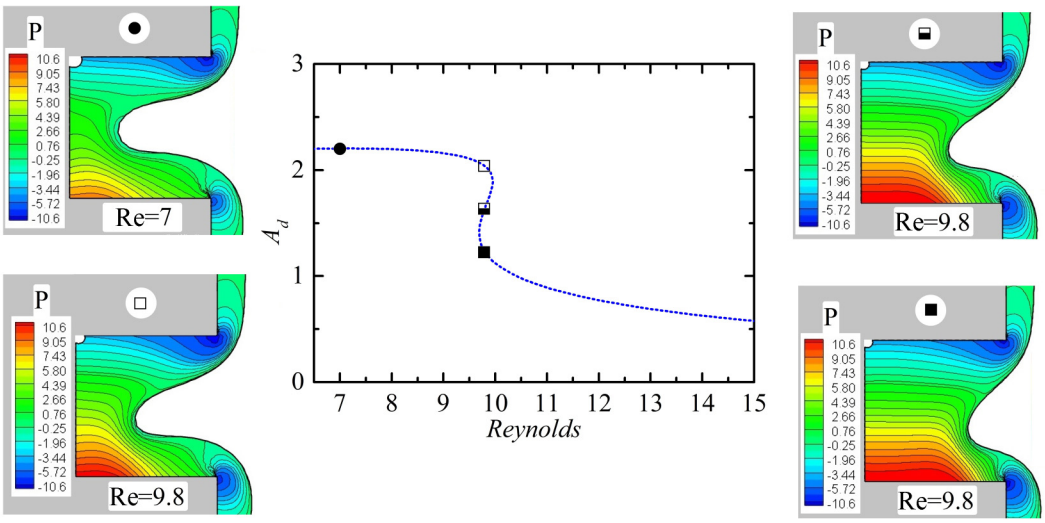

FIG. 10. Enlarged inertia-gravity zone (upper branch) for Ka $= 2$, $\theta = 60^\circ$, $d = 5$, and $w = 5$ along with contours of the pressure field for Re $= 7$ and Re $= 9.8$.

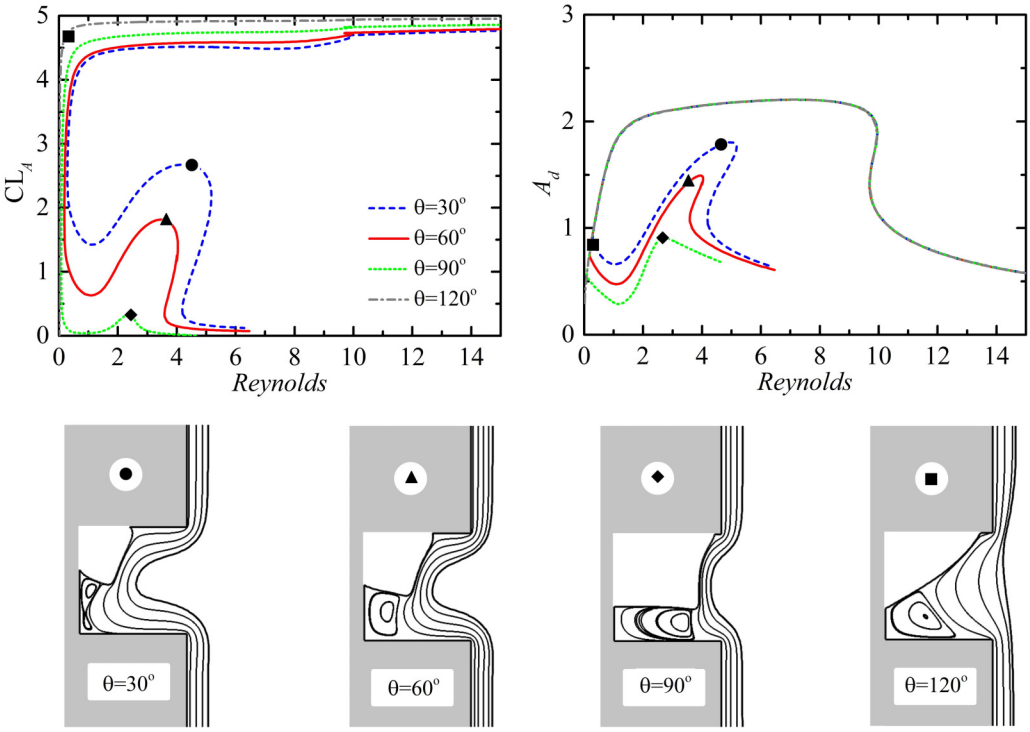

FIG. 11. Solution families for the wetting by contact line A (CL_A) or the deformation amplitude (A_d) for Ka = 2, $d = 5$, and $w = 5$ under different contact angles, along with certain film configurations.

increases. The fact that the two contact lines are unaffected by this intense change in the flow pattern as well as that the air inclusion is very small leads us to consider that a similar flow pattern could be obtained even in the absence of the air inclusion, i.e., in the case of full coating. Indeed, performing simulations in the absence of an air inclusion for the same parameter values, we found that the same hysteresis in A_d occurs as Re varies. This confirms our hypothesis that this "jump" in the deformation amplitude has to do only with the forces acting on the bulk and the outer free surface of the liquid (Fig. 7).

6. Effect of contact angle

Figure 11 presents the solution families of the wetting distance of CL_A and the deformation amplitude A_d for different contact angles as a function of Re. Clearly the extent of the liquid penetration and the film shape strongly depend on the contact angles, since the more hydrophilic the substrate the larger the force applied on the contact point, $F_{CL} = \sigma \cos(\theta)$. On the other hand, the contact angles do not affect qualitatively the bounds of the four regions defined and analyzed in the previous section. First, we will discuss small contact angles, $\theta = 30^\circ$. In comparison to the previous case with $\theta = 60^\circ$, the entire lower branch has moved upwards and to the right, while its variation with Re is stronger. As a result the local minimum in CL_A at the capillary-gravity region has moved to larger values and appears at slightly larger Re, while the upper turning point of the hysteresis loop is located at considerably higher Re and also CL_A reaches quite deeper into the trench before the hysteresis occurs. These observations can be explained by the fact that in more hydrophilic surfaces the liquid wets easier the trench and, thus, more inertia is needed to dominate over the capillary forces and moving the transition to the inertia region to higher values of flow rate and making the "hysteresis jump" more intense. Also, the deformation amplitude A_d intensifies, because deeper wetting of CL_A leads to increased values of the y component of velocity under the downstream

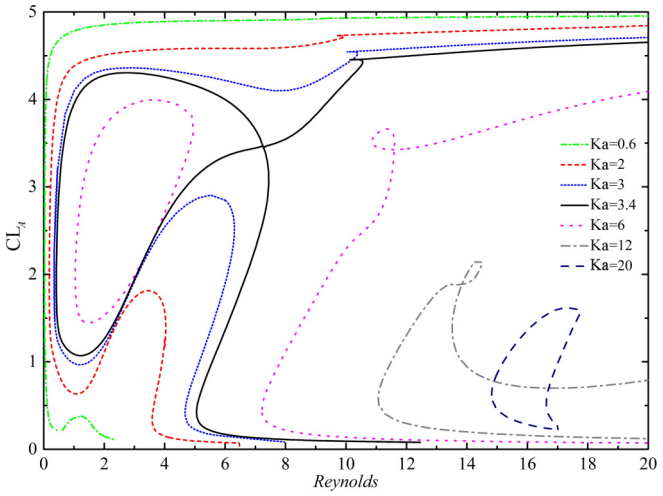

FIG. 12. Solution families for the wetting by contact line A (CL_A) for $\theta = 60^\circ$, $d = 5$, and $w = 5$ for different liquids characterized by their Ka.

wall, leading to sharper change in the direction of the velocity vector and larger stresses near the outer free surface. On the upper branch the smaller contact angle has very little effect on CL_A, while it has no effect on A_d. We have already mentioned that for this set of parameters the upper branch is unaffected by the location of the contact lines and the tiny air inclusion.

In the case of neutral contact angles, $\theta = 90^\circ$, we can see that the local minimum in the wetting length at the capillary-gravity region has moved almost to zero, as expected. Since the film deflection towards the trench is eliminated, here gravity pulls it almost vertically downwards. Hence, its shape varies only slightly, as also indicated by the very small values of A_d in this range of Re. CL_A is located near the upstream convex corner and the contact angle makes the interface normal to the wall minimizing the curvature and eliminating the pressure gradient across the film thickness, which would force it to enter the trench with increasing inertia. This results in no appreciable rise in the y component of velocity, lower stress components and considerably smaller increase in the deformation amplitude. Thus, the hysteresis loop vanishes as the transition from the capillary-gravity region to the inertia gravity region is very smooth, since the increasing inertia can be translated to just a raise in the film velocity. At $\mathrm{Re} = 4.6$, CL_A gets pinned on the upstream convex corner and the simulation stops. Again, the different contact angle has only a slight effect on the upper branch.

We also examined the flow over a hydrophobic substrate, $\theta = 120^\circ$. We observe that the lower branch does not exist anymore, since CL_A gets pinned on the upstream convex corner for all Re. The contact line length on the upper branch however, decreases monotonically and finally the contact point gets pinned on the upstream convex corner, i.e., $CL_A \to 0$ as $\mathrm{Re} \to 0$, before the saddle-node bifurcation on the capillary-gravity region occurs. As Re increases along the upper branch, the liquid penetrates further in the trench. The fact that we can find steady-state solutions with large penetration in a trench with a hydrophobic substrate, is in contrast with the transient coating simulations of Lampropoulos *et al.* [14], who found that the liquid never entered in a trench featuring a hydrophobic substrate but rather formed a Cassie-like state. Adding to this fact that no lower branch exists for a hydrophobic substrate, leads us to deduce that the upper branch is unstable.

7. Inertial effect for different liquids

Figure 12 presents the wetting distance of CL_A in terms of the Reynolds number for different liquids. We do not show the variations of CL_B or A_d for conciseness and because the solution families become quite complex. In practice, the Kapitza number varies mainly due to liquid viscosity, because

surface tension and density of common liquids do not vary as much. All liquids exhibit a drastic change of the wetting distance and deformation amplitude around a specific range of Reynolds number.

Initially we examine a liquid with less significant capillary effect (Ka = 0.6) than our base case (Ka = 2). In the lower branch there is no hysteresis loop, the minimum of CL_A at the capillary-gravity region is located at a lower Re and, generally, it has decreased for all Re. The first two observations can be explained by considering that the net force per unit of depth acting on CL_A and pulling the liquid into the trench is equal to $\sigma \cos\theta$. A decrease in the surface tension, when compared to the viscous effects, results in decreasing this force, thus, the transition from the capillary-gravity region to the inertia-gravity region is smoother and takes place earlier. The third observation similarly derives from of the fact that smaller Ka at a constant Re leads to a bigger Ca and thus to a less significant capillary effect. This moves the region bounds to lower values of the flow rate. This pattern resembles the one of increasing the contact angle, in fact both these changes in the fluid characteristics affect in the same way the solution family vanishing the hysteresis. Our simulation stops at Re = 3 because the neck of the film above the trench is so thin that the transformation cannot map any more the computational domain to the physical one, since the extremely deformed elements make the Jacobian of the transformation singular.

Next, we examine a liquid with slightly higher Kapitza number (Ka = 3) than our base case. We observe again that the trends are like those with decreasing the contact angle, for the reasons analyzed above. Slight further increase of Ka leads to dramatic changes in the flow patterns, because at Ka = 3.40875 a transcritical bifurcation occurs. We examine first the evolution of the lower branch. A relative increase in the capillary force leads on the one hand to deeper wetting of CL_A, and on the other advancing of CL_B because capillarity increases with respect to gravity moving higher the contact point on the bottom wall of the trench. As a result, the penetration of the liquid is increased and the flow patterns near the two contact points start to interact with each other. On the upper branch, the increased surface tension leads to less deformed inner and outer free surfaces, thus, less wetting of the upstream wall and larger air inclusion, until the two branches intersect forming a transcritical bifurcation at Ka = 3.40875.

For Ka = 6 we can observe in Figs. 12 and 13 that there is no continuous transition from the capillary-gravity region to the inertia-gravity region. The capillary-gravity zone now forms an isolated solution branch. Such so-called isolas are common in many types of nonlinear systems (Iooss and Joseph [39]) and film flows [20]. Here the isola is a product of the breaking of the transcritical bifurcation (Seydel [33]) forming two turning points, which separate the solution branches for lower Re from those for larger Re. For the range of $5 < \mathrm{Re} < 7.2$ no solutions exist for Ka = 6, while for $\mathrm{Re} > 7.2$ we can identify the inertia-gravity zone with two branches connected via a turning point at $\mathrm{Re} \approx 7.2$. As it can be seen in Fig. 12, the solution families in each region have the similar features after the breaking of the transcritical bifurcation. The same holds for the film shapes in nearby solution families before or after the bifurcation. The capillary-gravity region is bounded by two limit points, no transition zone exists and the two hysteresis loops at high Re have merged forming a sequence of three limit points at $\mathrm{Re} \approx 7.2$, $\mathrm{Re} \approx 11.6$, and $\mathrm{Re} \approx 10.9$.

Moving to even higher Kapitza numbers, the isola in the capillary-gravity region shrinks and eventually at Ka = 12 it ceases to exist. As the capillary effect becomes more significant than gravity, it is easier for the liquid to penetrate the trench and finally solutions partially filling it are not possible for low flow rates. Considering the inertia-gravity zone, while solutions for Ka = 6 extend to large Re, at higher Ka the two branches merge forming an isola, as seen at Ka = 20, which exhibits four turning points. Further increase of the Kapitza number eliminates all solutions with partial trench filling for all Reynolds numbers. This is in accordance with the flow maps of Lampropoulos *et al.* [14] who found full coating in a trench of this size ($d = 5$ and $w = 5$) by a liquid with Ka = 35. Note that with increasing the Kapitza number, side-wall effects would come into play, affecting the flow configuration, as suggested by Georgantaki *et al.* [40]. Future experimental studies should take under consideration that trenches should be wide enough in the third direction to achieve two-dimensional flow and examine liquids with higher Kapitza numbers than our base case.

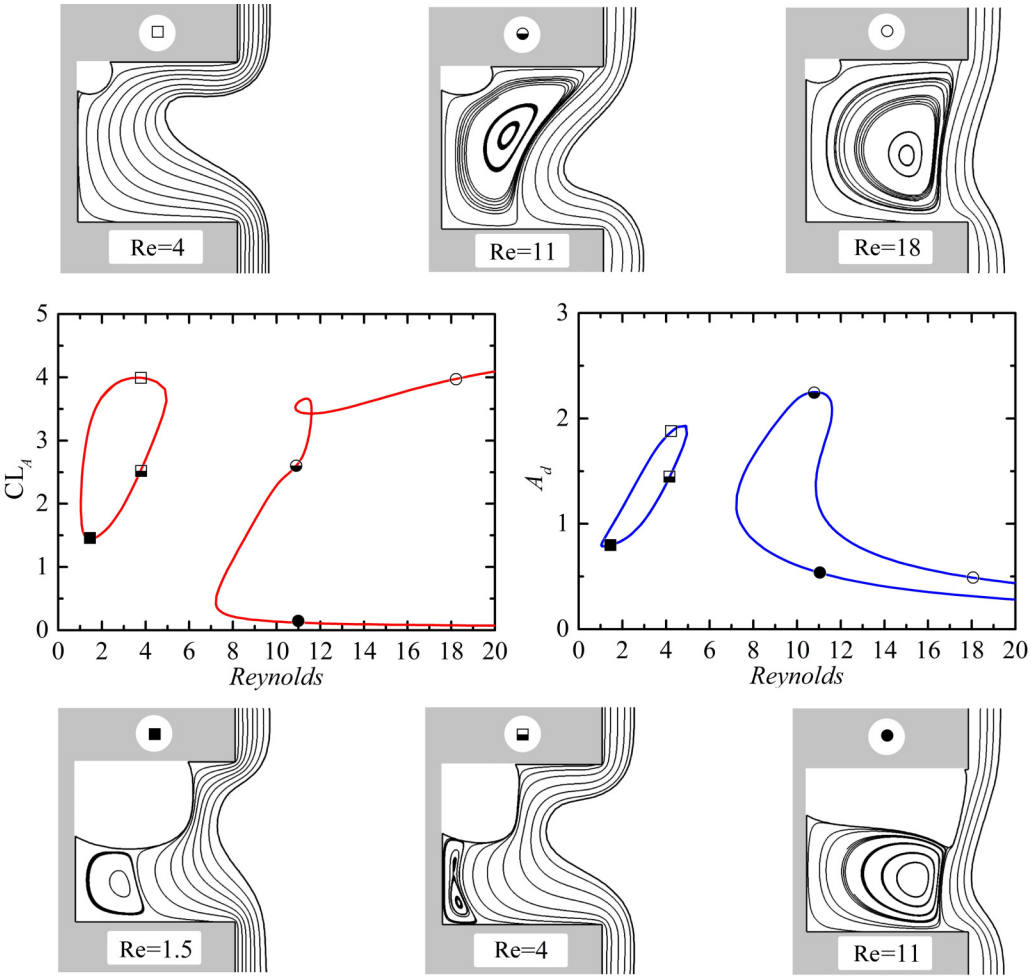

FIG. 13. Solution families for the wetting by contact line A (CL_A) or amplitude of deformation (A_d) for Ka = 6, $\theta = 60^\circ$, $d = 5$, and $w = 5$ along with film shapes and contours of the stream function.

Two very interesting observations, can be made if we plot the wetting length CL_A as a function of the Bond number Bo and the Weber number We, respectively. Figure 14 presents such diagrams for different Kapitza numbers. Examining CL_A as a function of Bo_m, we can observe that the saddle-node bifurcation in the capillary gravity region takes place at the same $Bo_m \approx 1.7$ for all Ka examined in this section. Note that the diagram is presented in semi-logarithmic scale to highlight this observation by locally expanding the position of the different turning points. In addition, $CL_A \approx 1.8$ at this turning point for all liquids. To explain the physics behind this observation, we introduce a simplified momentum balance in the film:

$$\frac{\rho U^2}{H} \approx \mu \frac{U}{H^2} + \rho g, \tag{16}$$

where $\frac{\rho U^2}{H}$ is the inertia force, $\mu \frac{U}{H^2}$ is the viscous force, and ρg is the gravity force. In the capillary-gravity region the inertia term is negligible and, thus, it is omitted from Eq. (16). To relate the viscous contribution with the capillary contribution we examine the normal stress balance. We note here that the local characteristic length, which scales the viscous forces in the area between the bubble and the outer region, is CL_A; this is the characteristic length normal to the main flow for

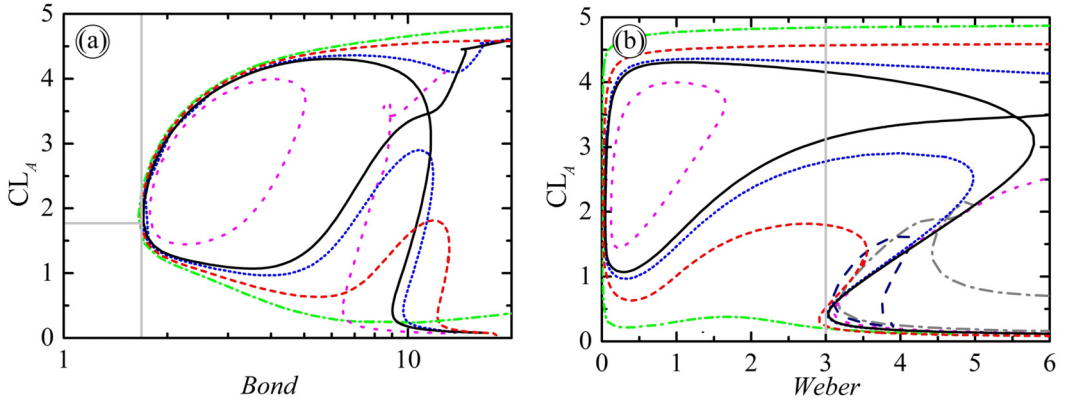

FIG. 14. Solution families in terms of CL_A as a function of (a) Bo_m and (b) We, for $\theta = 60^\circ$, $d = 5$, $w = 5$ for different liquids. The lines correspond to the same Ka as in Fig. 12.

negligible inertia. The curvature term is scaled by the width of the trench w. Having set the ambient air pressure to zero, we get

$$\mu \frac{U}{CL_A^*} \approx \frac{\sigma}{w}, \tag{17}$$

where CL_A^* is the dimensional wetting of contact line A. Neglecting the inertia term, combing Eqs. (16) and (17), and rearranging the terms, we get

$$\frac{\rho g H w}{\sigma} \approx \frac{CL_A^*}{H} \rightarrow \mathrm{Bo} \approx \mathrm{CL}_A. \tag{18}$$

Equation (18) indicates that at the limit of vanishing inertia force, CL_A should be of the same order of magnitude as the Bond number. This is clearly depicted in Fig. 14 (left), especially if we observe that at the turning point (lowest value of Bo for which solution of this type exists), the values of Bo and CL_A are almost the same, irrespective of the physical properties of each liquid.

Another relation between the different liquids can be made, if we notice that the inertia-gravity region arises at We = 3, regardless of the physical properties of each liquid. This has been also observed and explained in our previous work, where we studied the partial penetration flow of a viscous liquid over a slit; see Pettas *et al.* [16]. A criterion of entering the inertia-gravity region is obtained if we substitute the definition of the capillary number in the equation We = 3 and solve for Re_c. In fact, this critical Reynolds number is a function only of the physical properties of the liquid:

$$\mathrm{Re}_c = (3\mathrm{St}^{1/3}\mathrm{Ka})^{3/5}. \tag{19}$$

Simulations with bigger trenches, which will be presented in a next section, have proved that these relations are also independent of the geometry of the trench. However, we should mention that this relation is valid only for flow over hydrophilic substrates, because for hydrophobic ones these solution families do not exist.

8. Effect of the inclination angle

In many cases of coating processes, the inclination angle is not fixed at $\alpha = 90^\circ$. In Fig. 15 we present the impact of α on the flow profiles and on the evolution of the solution families as a function of the flow rate. For $\alpha = 80^\circ$ we observe a deeper wetting distance of CL_A, the capillary gravity region is found again in an isolated solution branch and there is no continuous transition to the inertia-gravity region. The x component of the gravity vector is weaker compared to the case of $\alpha = 90^\circ$, allowing CL_B to move closer to the upstream wall, while the y component of the gravity vector pushes more fluid inward the trench. Thus, we observe a smaller air inclusion. The fact that

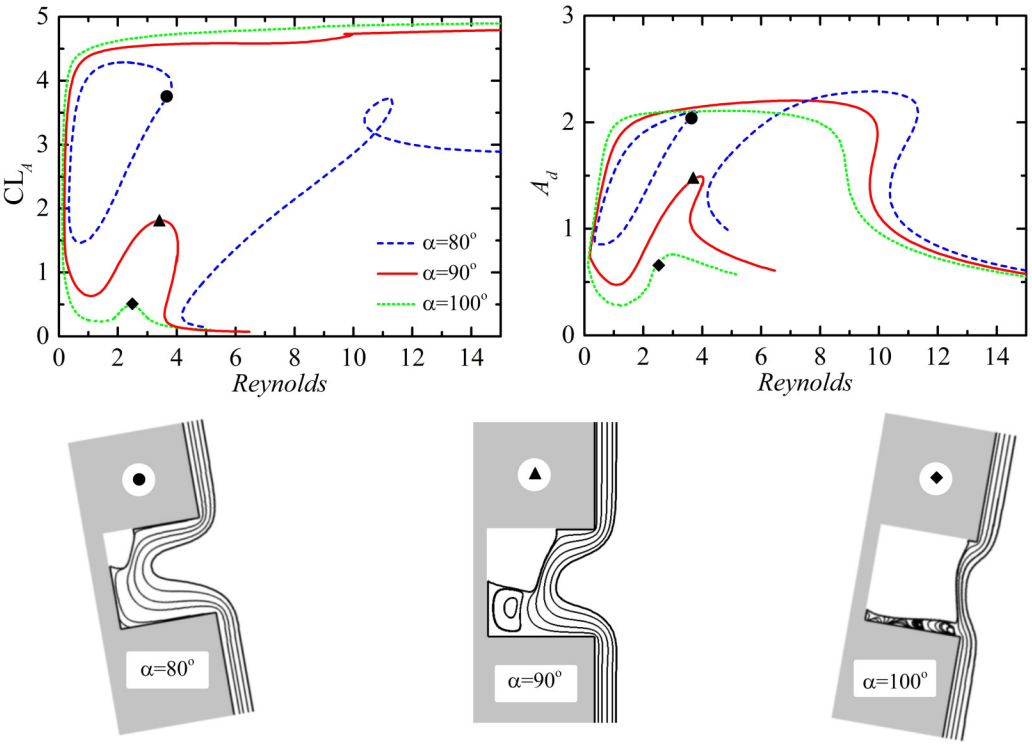

FIG. 15. Solution families in terms of CL_A or A_d, for $\mathrm{Ka} = 2$, $d = 5$, and $w = 5$ under different inclination angles along with film configurations.

the solution branches are disconnected is caused by the breaking of a transcritical bifurcation as discussed in the previous section. Further decrease of the inclination angle leads to a shrinkage of the isolated branch and a displacement of the inertia gravity region to higher Reynolds number, again like examining higher Kapitza numbers. In fact, for inclination angles lower than 68°, solutions of this type cease to exist. This observation is in qualitative agreement with the experiments of Schörner *et al.* [41,42]. They examined the flow of thin Newtonian films over sinusoidal substrates and rectangular trenches for liquids with $1.3 \leqslant \mathrm{Ka} \leqslant 3.7$ and inclination angles up to 36.7° and did not find any air inclusions even for high flow rates ($\mathrm{Re} \geqslant 30$). This fact is easy to interpret physically: For inclination angles less than 45° the y component of the gravity force will be dominant, and more effectively assist in filling the trench with liquid and, thus, will not allow air inclusions to be formed.

Increasing the inclination angle to $\alpha = 100°$ and examining the inertia effect leads to flow patterns with large air inclusions on the lower branch, because in this case gravity pulls liquid out from the trench. Both hysteresis loops on the lower branch and on the upper branch vanish. The effect of the inclination angle on the bifurcation curves resembles the effect of the Kapitza number. This can be justified by the fact that both parameters have a major effect on the balance of forces acting on the film close to the contact lines A and B.

9. Effect of the trench depth

In this section we investigate how the flow over patterned substrates is affected by different trench depth. In Fig. 16 the wetting distance of CL_A and the deformation amplitude A_d are plotted as a function of Re for different solution families corresponding to different depths of the trench. Examining the lower branch we see that increasing the trench depth from our base case of 5 has only a slight impact on either CL_A or A_d. Moreover, the insets in Fig. 16 also show that CL_B does

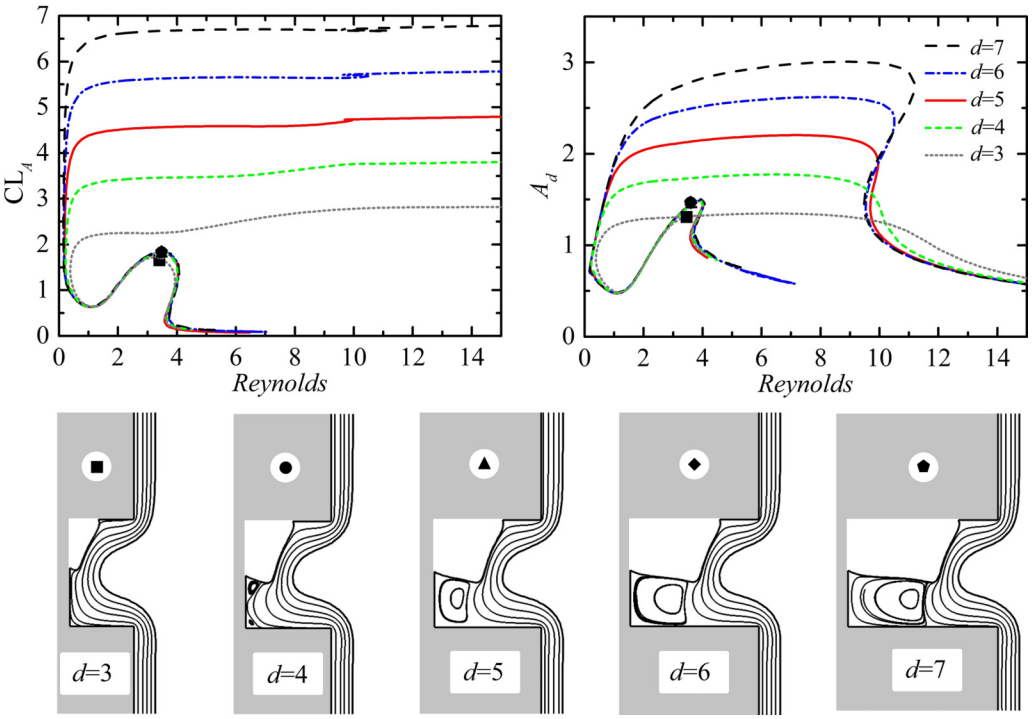

FIG. 16. Solution families in terms of wetting by contact line A (CL_A) or amplitude of deformation (A_d) for Ka $= 2$, $\theta = 60^\circ$, and $w = 5$ and different trench depths.

not change appreciably by increasing d from 5 to 7. All these are attributed to the fact that the recirculating region is large enough already at $d = 5$ and increasing the trench depth further affects only the liquid in the recirculating region, which, when it is large enough, plays almost no role on (a) the formation of the outer film profile, because it does not communicate with it and (b) the local force balance near point CL_B, where the flow remains much slower than in the outer film. On the upper branch of the solution family, however, the contact lines do not take part in the formation of the flow pattern as the air inclusion is always minimized around the upper convex corner and an increase of the trench depth (to the extent we have presented it here) at a constant Reynolds number simply leads to the outer free surface moving deeper into the trench (film profiles not shown for conciseness).

Decreasing the trench depth below 5 leads to vanishing of the upper branch hysteresis at high Re, because the outer free surface cannot abruptly change the depth to which it enters the trench, since the trench is too shallow to allow this. On the lower branch, a shallower trench has again a little effect, as we observe CL_A migrating slightly closer to the upstream convex corner and the outer free surface becoming slightly flatter. We also observe that CL_B migrates higher at the bottom of the trench as the recirculation region tends to vanish and contact line B interacts directly with the main stream of the flow.

10. Effect of the trench width

In contrast with the previous section, changing the trench width has a noteworthy effect on the flow characteristics, Fig. 17. Increase in the trench width above the base case of 5 moves the upper-branch hysteresis to higher values of the flow rate as more inertia is needed to move abruptly the minimum of the outer free surface deeper and closer to the downstream wall causing the "jump"

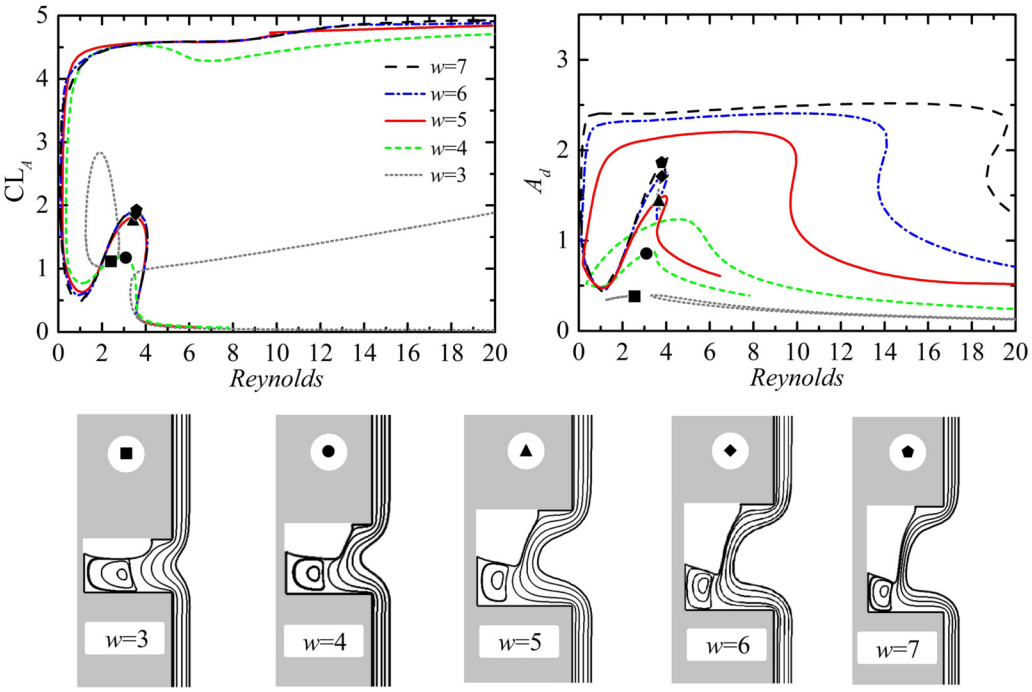

FIG. 17. Solution families in terms of the wetting by contact line A (CL_A) or amplitude of deformation (A_d) for Ka $= 2$, $\theta = 60^\circ$, and $d = 5$ and different trench widths.

on the deformation amplitude A_d as described in Sec. V A 5 (corresponding film shapes not given for conciseness).

On the lower branch, increase of w above 5 has a small effect on the wetting of CL_A, but affects considerably the deformation amplitude of the outer free surface which is in accordance with the ballistic effect mentioned in Sec. IV A 4 and makes thinner the part of the film freely falling.

Decreasing the width of the trench to $w = 4$ results in vanishing of the hysteresis in both branches since in the upper branch, the upstream wall comes close enough to the downstream wall and they do not allow the outer free surface to penetrate in the trench, while on the lower branch the transition is smoother. Further decrease of the trench width leads to a transcritical bifurcation and, when this is broken, to splitting again of the capillary-gravity from the inertia gravity region. This forms an isola and two new branches connected with a limit point as shown in Fig. 17 for $w = 3$.

B. Bubble formed in the upstream wall

In this section we examine the case in which contact line B is attached to the upstream wall and along with contact line A they are free to move remaining in contact to it. According to the flow maps of Lampropoulos *et al.* [14] this is not a common case of coating failure, since it is reported to take place for a very limited range of values of the parameters they examined. Figure 18 presents the wetting length of contact line A and the deformation amplitude of the outer free surface in terms of the Reynolds number. Here we observe that a single solution branch exists and seems to carry certain features of either the lower or the upper branch found in the case of a bubble in the upstream corner case. For example, it has two hysteresis loops. The first one is in the range of $5.8 < \mathrm{Re} < 8.2$, is clearer in CL_A and seems to correspond to the one in the lower branch in the previously studied cases, whereas the second hysteresis arises at higher Reynolds $9.6 < \mathrm{Re} < 9.8$, is clearer in A_d and resembles the one observed in the upper branch in Sec. V A.

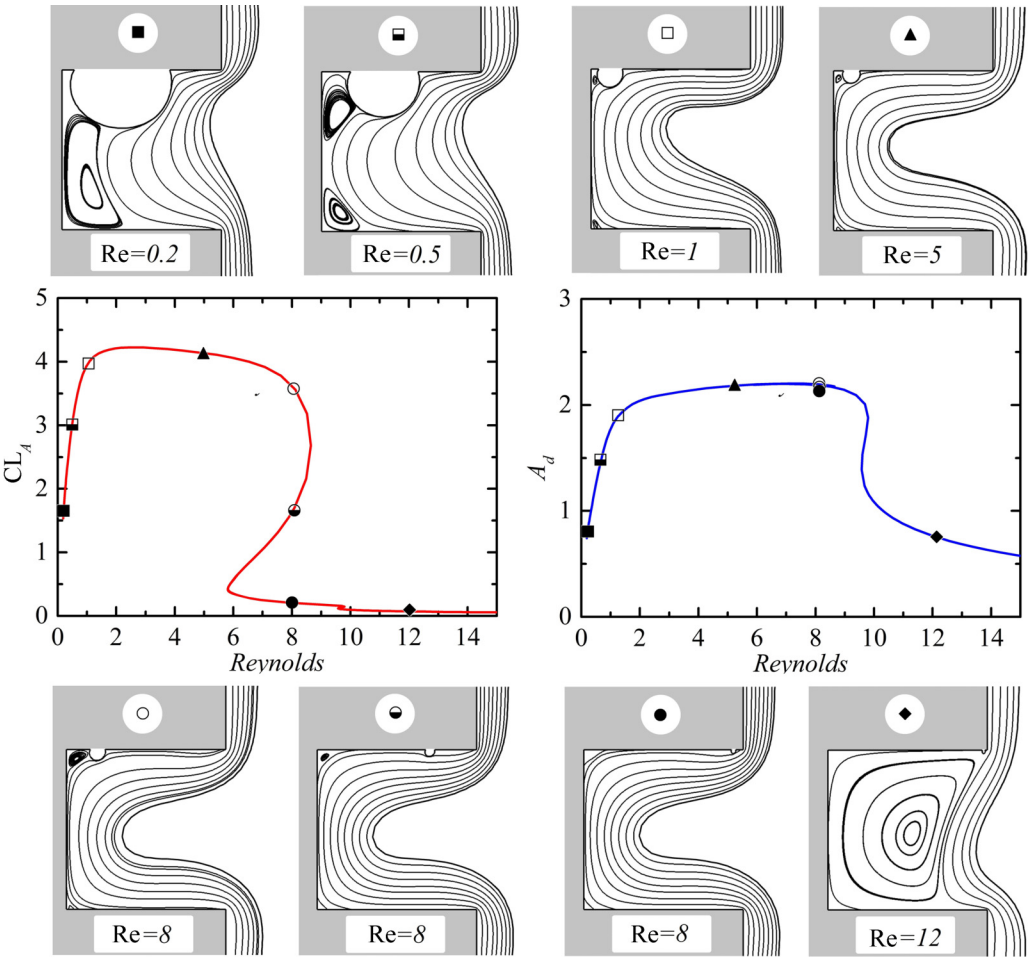

FIG. 18. Solution family in terms of CL_A or A_d, for $\mathrm{Ka} = 2$, $d = 5$, $w = 5$, and $\theta = 60^\circ$ along with film shapes and contours of the streamlines.

We could not extend the simulations for $\mathrm{Re} < 0.2$, because the bubble surface gets very close to the bottom of the trench and the elements mapping the fluid in this area become too deformed. As the flow rate increases so that the Reynolds number increases from $\mathrm{Re} \approx 0.2$ to $\mathrm{Re} \approx 0.5$ the wetting length from the convex corner in the upstream wall increases and the bubble size decreases so that the wetting length to the concave corner increases. Hence, the liquid occupies a larger area near the upstream concave corner, which allows for the previously larger recirculation covering most of the bottom of the trench to split in two smaller recirculations each one located in each concave corner. Increasing the flow rate further so that $\mathrm{Re} = 1$, we observe that the wetting length increases and the bubble size decreases considerably, while the size of both recirculations decreases. Up to this value of Re, these variations are the same as in the capillary-gravity region in the lower branch of the "bubble in the upstream corner" case, when inertia becomes more significant than viscous forces, so wetting of the upstream wall is facilitated. The increase in CL_A forces the bubble to move inwards and decrease in size, but CL_B cannot decrease below a certain value, because of the viscous forces developed between its surface and the bottom of the trench by the local recirculation. Simultaneously, the increased inertia causes a stronger deformation of the outer free surface.

For $1 < \mathrm{Re} < 8$ neither the bubble size nor the wetting lengths change appreciably, a pattern reminiscent of that in the upper branch in Sec. V A. For $\mathrm{Re} > 1$ the air inclusion has become so small that it does not affect the main flow or the outer film surface at all, on the contrary, it is affected by them. As the Reynolds number increases further, the first hysteresis loop is reached. This is generated by the increased inertia and the ballistic phenomenon, which moves the minimum in the outer free surface towards the downstream wall, increasing the area occupied by the liquid near the upstream wall and decreasing the pressure there. Both allow the bubble to migrate closer to the upstream corner sharply decreasing CL_A and increasing CL_B. Nevertheless, the first hysteresis loop has no effect on the main flow or the outer free surface, as it can be seen in the variation of A_d in Fig. 18. Further increasing Re leads to the second hysteresis loop, which can be more clearly observed when the solution family is depicted in terms of A_d. This is also attributed to the ballistic effect, which pushes the free surface minimum even closer to the downstream wall. There however, the flow needs to exit the trench, which decreases the size of this minimum drastically, generating the second hysteresis. At $\mathrm{Re} = 12$, the bubble is next to the upstream convex corner and most of the trench is occupied by a large liquid recirculation.

VI. CONCLUSIONS

The steady film flow of a Newtonian liquid has been studied over a trench of orthogonal cross-section examining the formation of either one of two types of air inclusion in contact with the trench walls. The contact lines of the inclusion are determined by imposing the angle at which the fluid detaches and reattaches to the solid wall. Gravity is the external force driving the flow, which is two-dimensional, assuming that the third distance of the trench is much larger. The mixed finite element method has been combined with a quasi-elliptic mesh generation scheme, which allows accurately capturing large deformations of the free surface of the fluid as it flows over the topography. Periodic conditions are imposed on velocity components, pressure, and position of the interface between the inflow and the outflow boundary.

The steady-state results are in very good agreement with those reported in previous observations and transient simulations. In this study, however, the evolution of entire solution families is presented in detail, as the flow rate, fluid properties trench geometry, and orientation are varied. A competition between capillary, viscous, and inertia forces gives rise to hydrodynamic hysteresis loops, which have been tracked in the parameter space using an arc-length-continuation algorithm. The mechanisms that lead to abrupt changes in the flow profiles have been explained in detail. Flow maps have been presented that demonstrate whether complete trench coating fails because a bubble is formed either in the upstream concave corner or in contact with the upstream wall, the two failure cases that arise most often. The coating quality can be improved mainly by increasing the Kapitza number. This can be implemented in a given liquid by increasing, for example, its temperature. Finally, using a more hydrophilic substrate or decreasing the inclination angle can also improve the coating quality.

The combined effect of inertia and viscoelasticity should be examined next, under partial wetting conditions following Pavlidis *et al.* [43] and Pavlidis *et al.* [44] who studied the corresponding full coating problem. The aspect of viscoelasticity is very important, as in most industrial applications the coating liquid is a viscoelastic solution. In a different direction, a linear stability analysis of the obtained steady-state solutions is necessary, as in Ref. [45], to definitively determine which configuration will prevail. This will be examined also in a forthcoming study.

ACKNOWLEDGMENTS

This work has been supported financially by the LIMMAT Foundation, under the Project "MuSiComPS," and the General Secretariat of Research and Technology of Greece through the program "Excellence" (Grant No. 1918, entitled "FilCoMicrA") in the framework "Education and Lifelong Learning" cofunded by the European Social Fund and National Resources. Dr. M. Pavlidis participated in the initial stage of this research.

[1] X. Yin and S. Kumar, Flow visualization of the liquid-emptying process in scaled-up gravure grooves and cells, Chem. Eng. Sci. **61**, 1146 (2006).
[2] K. Argyriadi, M. Vlachogiannis, and V. Bontozoglou, Experimental study of inclined film flow along periodic corrugations: The effect of wall steepness, Phys. Fluids **18**, 012102 (2006).
[3] R. V. Craster and O. K. Matar, Dynamics and stability of thin liquid films, Rev. Mod. Phys. **81**, 1131 (2009).
[4] J. Tsamopoulos, M. F. Chen, and A. Borkar, On the spin-coating of viscoplastic fluids, Rheol. Acta **35**, 597 (1996).
[5] L. E. Stillwagon and R. G. Larson, Leveling of thin films over uneven substrates during spin coating, Phys. Fluids **2**, 1937 (1990).
[6] A. Mazouchi and G. Homsy, Free surface stokes flow over topography, Phys. Fluids **13**, 2751 (2001).
[7] S. Kalliadasis, C. Bielarz, and G. M. Homsy, Steady free-surface thin film flows over topography, Phys. Fluids **12**, 1889 (2000).
[8] V. Bontozoglou and K. Serifi, Falling film flow along steep two-dimensional topography: The effect of inertia, Intl. J. Multiphase Flow **34**, 734 (2008).
[9] P. Tsai, A. M. Peters, C. Pirat, M. Wessling, R. G. H. Lammertink, and D. Lohse, Quantifying effective slip length over micropatterned hydrophobic surfaces, Phys. Fluids **21**, 112002 (2009).
[10] C. Kouris and J. Tsamopoulos, Dynamics of axisymmetric core-annular flow in a straight tube: I. The more viscous fluid in the core, bamboo waves, Phys. Fluids **13**, 841 (2001).
[11] P. Muralidhar, N. Ferrer, R. Daniello, and J. P. Rothstein, Influence of slip on the flow past superhydrophobic circular cylinders, J. Fluid Mech. **680**, 459 (2011).
[12] S. Moulinet and D. Bartolo, Life and death of a fakir droplet: Implement transitions on superhydrophobic surfaces, Eur. Phys. J. E **24**, 251 (2007).
[13] C. Duez, C. Ybert, C. Barentin, C. Cottin-Bizonne, and L. Bocquet, Dynamics of Fakir Liquids: From Slip to Splash, J. Adhension Sci. Technol. **22**, 335 (2008).
[14] N. K. Lampropoulos, Y. Dimakopoulos, and J. Tsamopoulos, Transient flow of gravity-driven viscous films over substrates with rectangular topographical features, Microfluid. Nanofluid. **20**, 51 (2016).
[15] G. Karapetsas, N. K. Lampropoulos, Y. Dimakopoulos, and J. Tsamopoulos, Transient flow of gravity-driven viscous films over 3D patterned substrates: Conditions leading to wenzel, cassie and intermediate states, Microfluid. Nanofluid. **21**, 17 (2017).
[16] D. Pettas, G. Karapetsas, Y. Dimakopoulos, and J. Tsamopoulos, On the degree of wetting of a slit by a liquid film flowing along an inclined plane, J. Fluid Mech. **820**, 5 (2017).
[17] Y. Dimakopoulos and J. Tsamopoulos, A quasi-elliptic transformation for moving boundary problems with large anisotropic deformations, J. Comp. Phys. **192**, 494 (2003).
[18] D. H. Michael, The separation of viscous liquid at a straight edge, Mathematika **5**, 82 (1958).
[19] S. Richardson, The die swell phenomenon, Rheol. Acta **9**, 193 (1970).
[20] S. F. Kistler and L. E. Scriven, The teapot effect: Sheet-forming flows with deflection, wetting and hysteresis, J. Fluid Mech. **263**, 19 (1994).
[21] R. E. Johnson and R. H. Dettre, Wettability and contact angles, in *Surface and Colloid Science*, Vol. 2, edited by E. Matijevic (Wiley-Interscience, New York, 1969), p. 85.
[22] J. F. C. Oliver and S. G. Mason, Resistance to spreading of liquids by sharp edges, J. Colloid Interface Sci. **59**, 568 (1977).
[23] G. F. Teletzke, H. T. Davis, and L. E. Scriven, Wetting Hydrodynamics, Rev. Phys. Appl. **23**, 989 (1988).
[24] F. R. Young, *Cavitation* (McGraw-Hill Book Company, New York, 1989).
[25] K. J. Ruschak, A method for incorporating free boundaries with surface tension in finite element fluid flow simulations, Int. J. Num. Meth. Eng. **15**, 639 (1980).
[26] C. Kouris and J. Tsamopoulos, Core-annular flow in a periodically constricted circular tube. Part 2. Nonlinear dynamics, J. Fluid Mech. **470**, 181 (2002).
[27] C. Pozrikidis, The flow of a liquid film along a periodic wall, J. Fluid Mech. **188**, 275 (1988).
[28] M. Pavlidis, Y. Dimakopoulos, and J. Tsamopoulos, Fully developed flow of a viscoelastic film down a vertical cylindrical or planar wall, Rheol. Acta **48**, 1031 (2009).

[29] N. Chatzidai, A. Giannousakis, Y. Dimakopoulos, and J. Tsamopoulos, On the elliptic mesh generation in domains containing multiple inclusions and undergoing large deformations, J. Comp. Phys. **228**, 1980 (2009).

[30] Y. Dimakopoulos and J. Tsamopoulos, Transient displacement of a newtonian fluid by air in straight or suddenly constricted tubes, Phys. Fluids **15**, 1973 (2003).

[31] E. J. Doedel, V. Romanov, R. C. Paffenroth, H. B. Keller, D. J. Dichmann, J. Galan-Vioque, and A. Vanderbauwhede, Elemental Periodic Orbits associated with the Libration Points in the Circular Restricted 3-Body Problem, Int. J. Bifurcat. Chaos Appl. Sci. Eng. **17**, 2625 (2007).

[32] A. Gupta, WSMP: Watson Sparse Matrix Package (Part-II: direct solution of general sparse systems), IBM Technical Report RC 21888, 98472 (2000).

[33] M. Zacharioudaki, C. Kouris, Y. Dimakopoulos, and J. Tsamopoulos, A direct comparison between volume and surface tracking methods with a boundary-fitted coordinate transformation and third-order upwinding, J. Comput. Phys. **227**, 1428 (2007).

[34] D. Fraggedakis, C. Kouris, Y. Dimakopoulos, and J. Tsamopoulos, Flow of two immiscible fluids in a periodically constricted tube: Transitions to stratified, segmented, churn, spray or segregated flow, Phys. Fluids **27**, 082102 (2015).

[35] H. K. Moffatt, Viscous and resistive eddies near a sharp corner, J. Fluid Mech. **18**, 1 (1963).

[36] R. Seydel, Practical bifurcation and stability analysis, *Interdisciplinary Applied Mathematics 5*, 2nd ed. (Springer-Verlag, New York, 1994).

[37] C. M. Gramlich, A. Mazouchi, and G. M. Homsy, Time-dependent free surface Stokes flow with a moving contact line. II. Flow over wedges and trenches, Phys. Fluids **16**, 1660 (2004).

[38] P. K. Nguyen and V. Bontozoglou, Steady solutions of inertial film flow along strongly undulated substrates, Phys. Fluids **23**, 052103 (2011).

[39] G. Iooss and D. D. Joseph, *Elementary Stability and Bifurcation Theory* (Springer-Verlag, New York, 1980).

[40] A. Georgantaki, J. Vatteville, M. Vlachogiannis, and V. Bontozoglou, Measurements of liquid film flow as a function of fluid properties and channel width: Evidence for surface-tension-induced long-range transverse coherence, Phys. Rev. E **84**, 026325 (2011).

[41] M. Schörner, D. Reck, and N. Aksel, Stability phenomena far beyond the Nusselt flow—Revealed by experimental asymptotics, Phys. Fluids **28**, 022102 (2016).

[42] M. Schörner, D. Reck, and N. Aksel, Does the topography's specific shape matter in general for the stability of film flows? Phys. Fluids **27**, 042103 (2015).

[43] M. Pavlidis, Y. Dimakopoulos, and J. Tsamopoulos, Steady viscoelastic film flow over 2D topography: I. The effect of viscoelastic properties under creeping flow, J. Non-Newt. Fluid Mech. **165**, 576 (2010).

[44] M. Pavlidis, G. Karapetsas, Y. Dimakopoulos, and J. Tsamopoulos, Steady viscoelastic film flow over 2D topography: II. The effect of capillarity, inertia and substrate geometry, J. Non-Newt. Fluid Mech. **234**, 201 (2016).

[45] D. Pettas, G. Karapetsas, Y. Dimakopoulos, and J. Tsamopoulos, On the origin of extrusion instabilities: Linear stability analysis of the viscoelastic die swell, J. Non-Newt. Fluid Mech. **224**, 61 (2015).